Journal of Cleaner Production 434 (2024) 140395

Contents lists available at ScienceDirect

Journal of Cleaner Production

journal homepage: www.elsevier.com/locate/jclepro

Thermo-optical characterization of novel MXene/Carbon-dot hybrid nanofluid for heat transfer applications

Sreehari Sreekumar [a,*], Abhijit Ganguly [b], Sameh Khalil [b], Supriya Chakrabarti [b], Neil Hewitt [a], Jayanta Deb Mondol [a], Nikhilkumar Shah [a]

[a] Centre for Sustainable Technologies (CST), Belfast School of Architecture and the Built Environment, Ulster University, Belfast, BT15 1ED, Northern Ireland, UK
[b] Nanotechnology and Integrated Bio-Engineering Centre (NIBEC), School of Engineering, Ulster University, Belfast, BT15 1ED, Northern Ireland, UK

ARTICLE INFO

Handling Editor: Panos Seferlis

Keywords:
Hybrid nanofluid
MXene
Carbon dot
Thermal conductivity
Volumetric heat capacity

ABSTRACT

Nanofluid has emerged as a promising heat transfer fluid (HTF) due to their significant thermophysical, and optical characteristics enhancement over base fluids. Hybrid nanofluids with multiple nanomaterials have the advantage of synergistic properties in comparison to monocomponent nanofluids. The present study proposes an energy-efficient and cleaner synthesis method for developing carbon quantum dot (C-dot), MXene, and a hybrid MXene/C-dot hybrid nanofluids, for heat transfer application. In-situ microwave pyrolysis technique and two-step method were adopted for nanomaterial and nanofluid synthesis. The morphological, phase structural, chemical, and elemental compositional analysis of the nanomaterials was performed. The material characterization confirms the hybridization of C-dot on MXene nanosheets. The thermal conductivity and volumetric heat capacity of the nanofluids were measured using the transient plane source (TPS) method. Thermal conductivity was observed to increase with nanofluid concentration and temperature. Results indicate that MXene has the highest thermal conductivity enhancement (50 %) over water, followed by hybrid (42.2 %) and C-dot nanofluid (33.2 %). The volumetric heat capacity of nanofluids decreased with concentration and temperature. A semi-empirical correlation, as a function of nanofluid concentration and temperature, was coined for predicting thermal conductivity and volumetric heat capacity. Optical property characterization study shows that C-dot nanofluid exhibited considerable absorption along the UV range, while MXene nanofluid showed absorption in the visible and near-infrared (NIR) region. Hybrid nanofluids demonstrated complementary absorption properties of C-dot and MXene nanofluids.

1. Introduction

Demand for efficient and compact energy conversion devices is driving the research to develop effective heat transfer systems. Conventional working fluids are commonly used in industrial and residential cooling and heating applications. Water, ethylene glycol (EG), propylene glycol, ionic liquids, and thermal oils, are some of the widely adopted working fluids (Sreekumar et al., 2022a). The thermal conductivity of these fluids is very low and hence, more efficient HTFs are required to enhance the heat transfer and thereby achieve size reduction in components. Nanofluids, developed by dispersing nanomaterials in base fluids, are found to possess exceptional thermophysical properties. They have the advantage of property tunability by augmenting nanoparticle shape, size, concentration, or material, which makes them flexible for specific applications (Xiong et al., 2021).

Metal (Cu, Al, Ag, Au, etc.), metal oxide (CuO, Al_2O_3, MgO, Fe_2O_3, ZnO, SiO_2, TiO_2), carbide (SiC, TiC, ZrC), nitride (AlN, SiN, TiN), and carbon nanomaterial (Graphene, CNT, MWCNT) based nanofluids were widely used in energy systems (Sreekumar et al., 2022b). Nanofluids find applications as HTF in heat exchangers (Ambreen et al., 2022), solar collectors (Sreekumar et al., 2019), electronic devices (Selvaraj and Krishnan, 2021), etc. Colloidal stability and cost associated with the nanofluid-based system are the major drawbacks faced. Carbon quantum dot (C-dot) nanofluids are a recently developed class of HTFs. Carbon-dot materials are being adopted in solar cells, composite synthesis, fluorescent devices, etc. Due to their exceptional optical characteristics (Kim et al., 2022; Li et al., 2023). However, lesser research attention was provided to the study the heat transfer and rheological properties of carbon quantum dot (C-dot) nanofluids. Mirsaeidi and

* Corresponding author. Centre for Sustainable Technologies (CST), Ulster University, Belfast Campus, Birley Building, BB-02-007, Belfast, County Antrim, BT15 1ED, Northern Ireland, UK.
E-mail address: s.sreekumar@ulster.ac.uk (S. Sreekumar).

https://doi.org/10.1016/j.jclepro.2023.140395
Received 18 October 2023; Received in revised form 17 December 2023; Accepted 24 December 2023
Available online 29 December 2023

Nomenclature

Parameters

C_p	Mass-specific heat capacity [$J\ kg^{-1}\ K^{-1}$]
$C_{p,vol}$	Volumetric heat capacity [$J\ kg^{-1}\ K^{-1}$]
$C_{p\ vol,C-dot}$	Volumetric heat capacity of C-dot [$J\ kg^{-1}\ K^{-1}$]
$C_{p\ vol,MXene}$	Volumetric heat capacity of MXene [$J\ kg^{-1}\ K^{-1}$]
$C_{p\ vol,hybrid}$	Volumetric heat capacity of MXene/C-dot [$J\ kg^{-1}\ K^{-1}$]
ew	Equivalent weight [$g\ equivalent^{-1}$]
k	Thermal conductivity [$Wm^{-1}K^{-1}$]
$k_{TC,C-dot}$	Thermal conductivity of C-dot [$Wm^{-1}K^{-1}$]
$k_{TC,MXene}$	Thermal conductivity of MXene [$Wm^{-1}K^{-1}$]
$k_{TC,MXene/C-dot}$	Thermal conductivity of MXene/C-dot [$Wm^{-1}K^{-1}$]
K_λ	Spectral specific extinction coefficient [cm^{-1}]
t	Time [s]
T	Temperature [$^\circ C$]
T_{C-dot}	Instantaneous temperature of C-dot nanofluid [$^\circ C$]
T_{MXene}	Instantaneous temperature of MXene nanofluid [$^\circ C$]
T_{hybrid}	Instantaneous temperature of MXene/C-dot nanofluid [$^\circ C$]
ΔT	Instantaneous temperature difference [$^\circ C$]
$\delta U_{\alpha_{th}}$	Uncertainty in thermal diffusivity calculation [%]
δU_e	Uncertainty in measurement instrument [%]
δU_k	Uncertainty in thermal conductivity calculation [%]
δU_r	Uncertainty due to repeatability [%]
y	Penetration depth [m]

Greek Symbol

α_{th}	Thermal diffusivity [m^2s^{-1}]
ρ	Density [kgm^{-3}]
φ	Weight percentage [%]
τ_λ	Spectral-specific transmittance percentage [%]
λ	Wavelength [nm]
δ	Uncertainty [%]

Abbreviations

ACS	American chemical society
AM	Air mass
ANOVA	Analysis of variance
BE	Binding energy
CuO	Copper oxide
C-dot	Carbon quantum dot
DI	De-ionized
DAPTC	Direct absorption parabolic trough collector
DASC	Direct absorption solar collector
EIS	Electrochemical impedance spectroscopy
EG	Ethylene glycol
EDX	Energy dispersive X-ray
FE-SEM	Field emission scanning electron microscope
IPA	Isopropyl alcohol
ISO	International organization for standardization
JCPDS	Joint Committee on Powder Diffraction Standards
HTC	Heat transfer coefficient
HTF	Heat transfer fluid
MWCNT	Multi-walled carbon nanotube
NIR	Near-infrared
PV/T	Photovoltaic/thermal
SEM	Scanning electron microscopy
TPS	Transient plane source
UV	Ultraviolet
XPS	X-ray photoelectron spectroscopy
XRD	X-Ray diffraction

Yousefi (2021) conducted an experimental study on the thermal conductivity, viscosity and density of carbon dot nanofluid and a new semi-empirical correlation was derived to predict the properties. Ultra-stable C-dot nanofluids were developed by microwave-irradiation for application in optical nanofluid filter-based photovoltaic/thermal system (Xiao et al., 2023). The study reveals that the optical property of C-dot helped the system to outperform the existing nanofluid filters. The major drawback faced by C-dot nanofluid is the relatively lower thermal performance enhancement when compared to its exceptional stability and optical characteristics (Vatani et al., 2019).

Apart from C-dots, MXene is a newer class of 2D materials that finds application in energy storage, batteries, supercapacitors, catalysts, etc (Abbasi et al., 2021). In addition to their optical, and electrical properties, MXene colloidal solutions possess exceptional thermal conductivity, which is very less explored in past studies (Bao et al., 2021). Bao et al. (2021) synthesized $Ti_3C_2T_x$ MXene nanofluid dispersed in EG. Thermal conductivity of 5 vol % multi-layered and single-layered nanofluid increased by about 53.1 and 64.9 %, respectively. The viscosity of 1 vol % of MXene was observed to be lower than that of graphene and MWCNT nanofluids of 0.1 vol % due to the self-lubricating property of the MXene nanosheet. Thermophysical properties of ionic liquid-based MXene nanofluid were analysed by Das et al. (2020) for application in a photovoltaic/thermal (PV/T) system. The study shows that the PV/T system produces better thermal performance at an optimum concentration of 0.2 wt %. The feasibility of MXene nanofluid for heat transfer enhancement in a pin-fin heat sink was conducted by Ambreen et al. (2022). The study shows that about 40 % enhancement in the average Nusselt number was achieved with the nanofluid coolant at the expense of a very small increase in pumping pressure. Hence, majority of studies report that MXene nanofluid exhibits better thermal conductivity and heat transfer enhancement.

Hybrid nanofluids consisting of two or more nanomaterial shows synergistic properties in comparison to monocomponent nanofluids (Siddiqui et al., 2019; Sreekumar et al., 2019). Hybrid nanofluids could be synthesized using either a one-step method (Joseph and Thomas, 2022) or a two-step method (Said et al., 2023). The nanomaterial shape/size, nanofluid concentration, and mixing ratio (Xuan et al., 2022) are the other dominant factors that determine the bulk thermophysical properties of the hybrid nanofluid. An EG based SiC–ZnO hybrid nanofluid synthesized by Ghafouri and Toghraie (2023) exhibited about 15.9% enhancement in thermal conductivity over base fluid. A hybrid mixture of an ionic liquid and water was used as the base fluid by Said et al. (2022) for synthesising MXene hybrid nanofluid. The study reports that the thermal conductivity improved from 0.443 to 0.82 $Wm^{-1}K^{-1}$ for 0.5 wt % nanofluid concentration. Das et al. (2022) developed a Therminol 55-based MXene/Al_2O_3 nanofluid and the characterization was performed for three different concentrations of the fluid. The thermal conductivity of base fluid was found to be enhanced by 62 % with 0.2 wt % of nanoparticle loading. High thermally conductive copper nanomaterial was hybridized with C-dot nanoparticle by Azizi et al. (2018) to generate Cu/C-dot hybrid nanofluid. The nanofluid exhibited complementary thermal conductivity enhancement of around 25 % at 0.5 wt %, and high dispersion stability. MXene was found to be one of the better thermally conductive nanomaterials with potential for hybridization.

The literature review shows that the research performed on C-dot, and MXene nanofluids is very rare. C-dot nanofluids exhibits significant stability and optical property, in comparison to thermal property enhancement. While MXene nanofluid exhibits high thermal conductivity enhancement. The literature study reveals that a hybrid nanofluid could show synergistic characteristics of the component nanomaterials (Siddiqui et al., 2019). To the best of authors knowledge, a hybrid

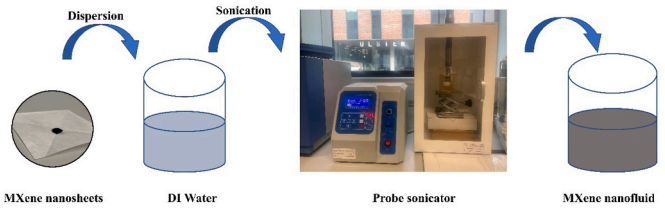

Fig. 1. Synthesis of MXene nanofluid.

MXene/C-dot nanofluid has not been reported to date. Hence, a novel hybrid MXene/C-dot nanofluid was synthesized as an alternative, and stable HTF with synergistic thermal and optical properties. Characterizations were performed on all the nanofluids of five different concentrations (0.01–0.2 wt %) and an effective comparison was conducted with monocomponent nanofluids. In this study, morphological, phase structure, and chemical compositional analysis was performed on the novel MXene/C-dot hybrid nanomaterial. Optical and thermophysical property characterization of C-dot, MXene, and MXene/C-dot nanofluids were also conducted for the very first time in this study. Based on the measured values of thermal conductivity and volumetric heat capacity, a new semi-empirical correlation was coined to predict these properties based on the nanofluid concentration and temperature.

2. Materials and methodology

The raw materials required for nanomaterial and nanofluid synthesis are detailed in this section. The synthesis procedure, synthesis equipment used, characterization equipment, and characterization methodology adopted for nanomaterial/nanofluid are also explained.

2.1. Materials required

De-ionized (DI) water was used as the base fluid for dispersing nanomaterials. Ammonium citrate dibasic (Merck, UK 247561) of ACS reagent grade (98 % purity), was used as the carbon source for carbon quantum dot nanofluid synthesis. Multi-layered MXene nanosheets of 99 wt % purity were procured from NanoChemazone, Canada and were used without further purification. Further details of the raw material are provided in Table S1 in **Section S1** of the supplementary data file.

2.2. Nanofluid synthesis methodology

The synthesis methodology adopted for developing C-dot, MXene, and MXene/C-dot nanofluids is detailed in this section. Five different concentrations of each nanofluid (0.01, 0.05, 0.1, 0.15, and 0.2 wt %) were synthesized. The optimum concentration that generates the maximum thermal conductivity improvement with minimum viscosity, was selected as the upper limit for nanofluid concentration (0.2 wt %) in this study (Mahesh et al., 2016; Parashar et al., 2021). The lower limit of nanofluid concentration (0.01 wt %) was selected such that the fluid samples are capable of exhibiting minimum thermal conductivity enhancement of about 5% (at 20 °C).

2.2.1. Synthesis of MXene nanofluid

A two-step method was adopted for MXene nanofluid synthesis as shown in Fig. 1. Firstly, the multi-layered MXene nanofluids were dispersed in the DI water without any surface modifiers using an Ultrasonic homogeniser. Sonication was found to be effective in delaminating the MXene sheets (Feng et al., 2018). The nanofluid was subjected to sonication for about 30 min of sonication time. Previously reported works from the literature was analysed to develop a preliminary understanding on the range of sonication time used for MXene delamination (Zhang et al., 2017). Sonication time selected in this study was found to be the lowest time taken to achieve delamination of MXene layers. MXene nanofluid of five concentrations (0.01–0.2 wt %) was synthesized.

2.2.2. Synthesis of carbon quantum dot nanofluid

A two-step method was adopted to prepare carbon quantum dot nanofluid. Ammonium hydrogen-citrate precursor (2 g) dissolved in DI-water (10 ml) is to be subjected to microwave treatment, as shown in Fig. 2, at 180 °C for about 10 min (Ettefaghi et al., 2018). A domestic microwave of 800 W capacity was used for the synthesis. The solution is to be further dried and cooled to room temperature. The synthesis process parameters were varied to find the optimum conditions for synthesising the C-dot in this study. Carbon dot nanoparticles are collected after the process. The collected particles are further dispersed in the base fluid at a different mass fraction (0.01–0.2 wt %) to synthesize the nanofluids.

2.2.3. Synthesis of MXene/Carbon quantum dot hybrid nanofluid

In-situ microwave-assisted synthesis (Zheng et al., 2018) of hybrid nanocomposite nanofluid was performed as shown in Fig. 3. Microwave irradiation has been reported to be a sustainable, less energy-intensive, and cost-effective synthesis route for various nanocomposite materials including MXene (Zheng et al., 2019) and C-dot (Meng et al., 2020) based nanocomposites. In this procedure, 2 g of ammonium

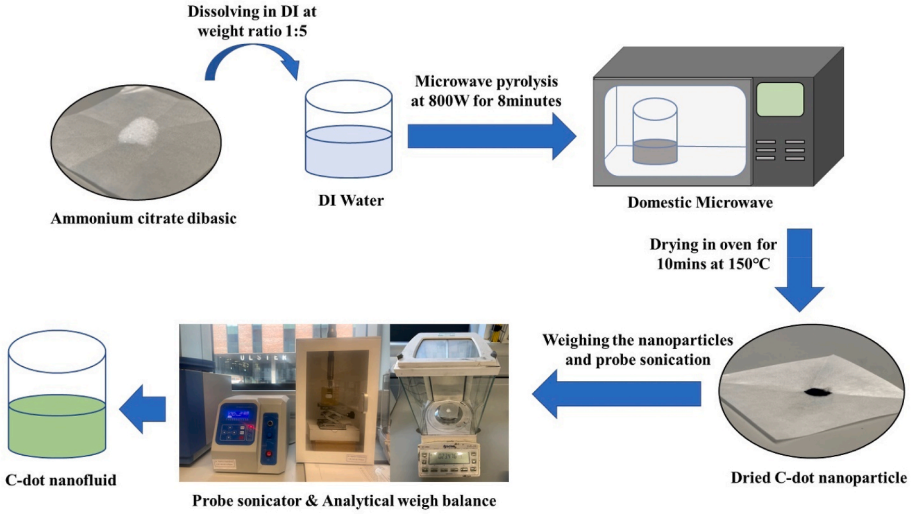

Fig. 2. Synthesis of C-dot nanofluid.

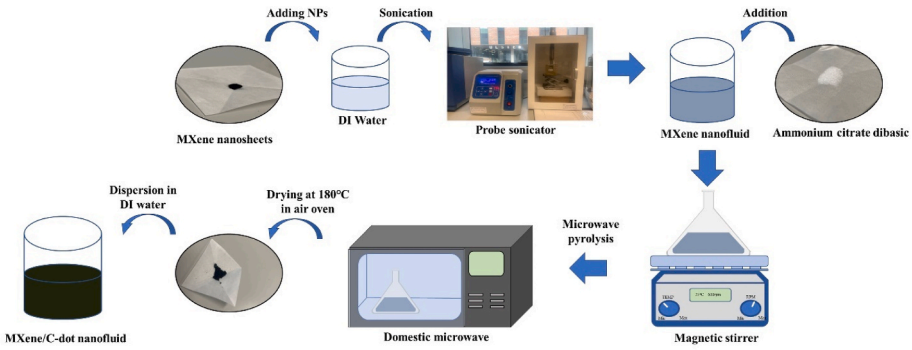

Fig. 3. Synthesis of MXene/C-dot hybrid nanofluid.

hydrogen-citrate precursor (carbon source) was dissolved in DI water. To the above-prepared solution, 1 g of MXene nanoparticle was added and mixed thoroughly for 10 min. The component mixture was kept in a microwave oven for about 8 min at a power of about 800 W. A nanocomposite of MXene/C-dot was formed as shown in Fig. 3. The material was collected and dried at 180 °C for 10 min in an air dryer. The dried nanoparticles were dispersed in DI water to prepare MXene/C-dot hybrid nanofluid.

2.3. Nanomaterial characterization

The nanomaterial samples were deposited on silicon wafers for performing the material characterization. The sample preparation procedure is explained in **Section S1** of supplementary data file. The morphology of the nanomaterials was analysed using FESEM (HITACHI SU5000, Tokyo, Japan) at an accelerating voltage of 5 kV. Elemental mapping and chemical composition analysis of the nanomaterials were conducted using an FE-SEM coupled X-Max^N 80 mm^2 silicon drift detector. Phase structure analysis of MXene, C-dot, and hybrid MXene/C-dot nanoparticles was performed using Bruker D8-Discover X-Ray diffractometer with Cu Kα radiation source ($\lambda = 1.54$ Å) in the 2 θ angle range of 0–90° at a scanning rate of 2°/min. Raman spectrum analysis was also performed on the samples using Renishaw inVia Qontor Confocal Raman Microscope (Renishaw Ltd., UK). A laser source having an excitation wavelength of 532 nm was used to confirm the crystalline nature of synthesized C-dot and hybrid nanoparticles. The elemental composition of the nanomaterials was analysed using X-ray photoelectron spectroscopic (XPS) analysis.

2.4. Nanofluid characterization

Analysis of the bulk volume property of nanofluid is necessary as it determines its applicability in thermal or heat transfer systems. This section describes the methodology adopted to perform an effective thermal and optical property characterization of nanofluids.

2.4.1. Thermal property analysis

The thermal conductivity, thermal diffusivity, and volumetric specific heat are the three thermal characteristics of the fluids that were analysed using a thermal constant analyser (Hot disk TPS-2500, Sweden). Thermal conductivity analysis of all 15 samples was performed using the Kapton-7577F1 sensor at the same heating power (25 mW) and with equal measurement time (4 s). The experimental test rig for temperature-dependent thermal property characterization is shown in Fig. S3 in the Supplementary data file. An exploded view depicting the sensor arrangement inside the liquid sample holder of the thermal conductivity analyser was exhibited in Fig. S4 of the Supplementary data file. Properties were evaluated within the temperature range of a typical low-temperature solar collector (20–60 °C). Thermal conductivity and thermal diffusivity values are directly obtained from the analysis. Equation (1) depicts the relation between thermal diffusivity, conductivity, and volumetric heat capacity of the fluid. The volumetric heat capacity of nanofluid was calculated from the measured thermal conductivity and thermal diffusivity values.

$$\alpha_{th} = \frac{k}{(\rho C_p)} = \frac{k}{C_{p,vol}}\ m^2 s^{-1} \tag{1}$$

In the above equation k (Wm^{-1}K^{-1}), ρ (kgm^{-3}), C_p (kJkg^{-1}K^{-1}), $C_{p,vol}$ (kJm^{-3}K^{-1}) represents the thermal conductivity, density, specific heat capacity, and volumetric heat capacity, respectively. Using the experimental data, a new correlation was proposed for predicting the temperature-dependent thermal conductivity and volumetric-specific heat of each nanofluid. The accuracy and methodology of measurement were validated by comparing the measured thermal conductivity values of a reference liquid with the experimentally reported data (Sandhu and Gangacharyulu, 2017) as shown in Fig. S5 in the Supplementary data file. The relative variation of the measured values from reference data was calculated and found to be falling within 5 %.

2.4.2. Optical property analysis

The transmittance of the nanofluid was measured using a UV–Vis–NIR spectrometer (PerkinElmer Lambda 650S) with a 150 mm integrating sphere. Spectroscopic analysis was conducted in standard transmittance mode and followed by using an integrating sphere, to effectively calculate the spectral absorption and scattering coefficient. The scattering coefficient was calculated to account for the attenuation of the beam in the nanofluid due to scattering. Beer-lambert law as shown in Equation (2) correlates the measured transmittance (τ_λ) with extinction (K_λ). Extinction coefficient was measured using Equation (3) (Huang et al., 2022).

$$\tau_\lambda = e^{-K_\lambda \cdot l} \tag{2}$$

$$k_\lambda = -\frac{1}{l}\ln(\tau_\lambda) \tag{3}$$

In the above equations, l indicates the optical path length of the quartz tube (1 cm).

2.5. Uncertainty analysis

An uncertainty analysis was performed to estimate the error involved in the experimental determination of thermal conductivity, thermal diffusivity, and volumetric heat capacity of nanofluids. The uncertainty involved with data measured using an instrument depends on the uncertainty of the measurement instrument (δU_e), and the uncertainty due to its repeatability (δU_r) (Ebrahimnia-Bajestan et al., 2016). The general formula for calculating the uncertainty is shown in Equation (4). As the thermal conductivity and thermal diffusivity were directly measured using the instrument, the uncertainty was calculated using Equations (5) and (6), respectively. Volumetric heat capacity being a function of

Table 1
Results from uncertainty analysis.

Equipment	Uncertainty
Thermal conductivity	±2.24 %
Thermal diffusivity	±3.19 %
Volumetric heat capacity	±3.90 %

thermal conductivity and diffusivity, the Moffat method (Pesteei et al., 2005) was used for the error analysis as shown in Equation (7).

$$\delta U = \sqrt{\delta U_e + \delta U_r} \tag{4}$$

$$\delta U_k = \sqrt{\delta U_{e,k} + \delta U_{r,k}} \tag{5}$$

$$\delta U_{\alpha_{th}} = \sqrt{\delta U_{e,\alpha_{th}} + \delta U_{r,\alpha_{th}}} \tag{6}$$

$$\delta C_{p,vol} = \sqrt{\left(\frac{\partial C_{p,vol}}{\partial k}\delta U_k\right)^2 + \left(\frac{\partial C_{p,vol}}{\partial \alpha_{th}}\delta U_{\alpha_{th}}\right)^2} \tag{7}$$

In the above equations, δU_k, $\delta U_{\alpha_{th}}$, and $\delta(\rho C_p)$ represents the uncertainty in the measurement of thermal conductivity, thermal diffusivity, and volumetric heat capacity, respectively. The accuracy of Hot Disk TPS 2500S in measuring thermal conductivity and thermal diffusivity was better than ±5 and ±10%, respectively (Hot disk instruments, 2015). The respective repeatability of results was about ±0.055 and ±0.22% (Hot disk instruments, 2015). The result from the analysis, as shown in Table 1, states that maximum uncertainty in the calculations falls within ±4%. Hence, the errors involved in the thermal conductivity, thermal diffusivity, and volumetric heat capacity measurement were minimal.

3. Results and discussion

Nanomaterial and nanofluid characterization data was analysed and observations are explained in this section.

3.1. Morphological analysis

Fig. 4 shows the morphology of the carbon dot, MXene and MXene/C-dot nanomaterials under study. Fig. 4 (a) visualises the SEM image of C-dot nanoparticles. The drop-casted materials (from a colloidal solution of C-dot nanoparticles in water) on silicon substrates exhibited a "gel" formation, resulting in a thin layer of "insulating" gel-like film covering the highly conducting C-dots. Because of the unavoidable "charging effect" from the "insulating" coverage, it was not possible to get any magnified SEM image. Fig. 4 (b) shows the MXene nanosheet arrangement. The morphology of the hybrid nanomaterial as observed in Fig. 4 (c), shows that the carbon nanoparticles are deposited on the MXene nanosheets. The magnified image shown in Fig. 4 (d) reveals the distribution of C-dot nanoparticles on the basal planes of the MXene nanosheet. As observed, the average size of the C-dots falls within the 8–20 nm range. The C-dot particle morphology agreed with previously reported studies with comparatively smaller sizes (Ahmadian-Fard-Fini et al., 2018; Hatimuria et al., 2023).

3.2. Chemical compositional analysis

Elemental mapping of C-dot, MXene, and MXene/C-dot nanomaterials are shown in Figs. 5–7, respectively. As inferred from Fig. 5, the significant elements detected during the mapping of C-dot nanoparticles are C, O, and N which constitute about 65.4, 19.7, and 14.9 %, respectively. EDX analysis of MXene as shown in Fig. 6, indicates that titanium (Ti) is the major element contributing about 43.1 % of the total elemental composition. Followed by fluorine, carbon, oxygen, and trace amounts of Al. The presence of elements F and Al is caused due to the etching process performed on Ti3AlC2 using HF during the synthesis phase. As carbon is the common element in both materials, the elemental composition analysis of MXene/C-dot nanoparticle as observed in Fig. 7 shows a higher percentage of C (56.8 %), followed by O (19.6 %) and Ti (16.5 %).

3.3. Phase structure analysis

The XRD spectrum of each nanomaterial can be observed in Fig. 8. As

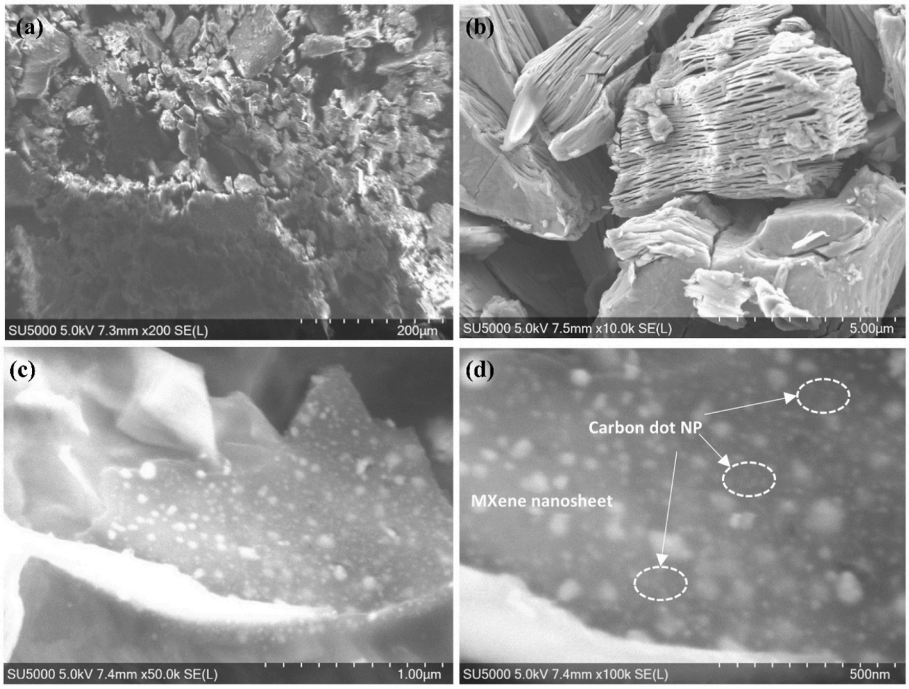

Fig. 4. SEM images of (a) C-dot (b) MXene (c) & (d) MXene/C-dot nanoparticle.

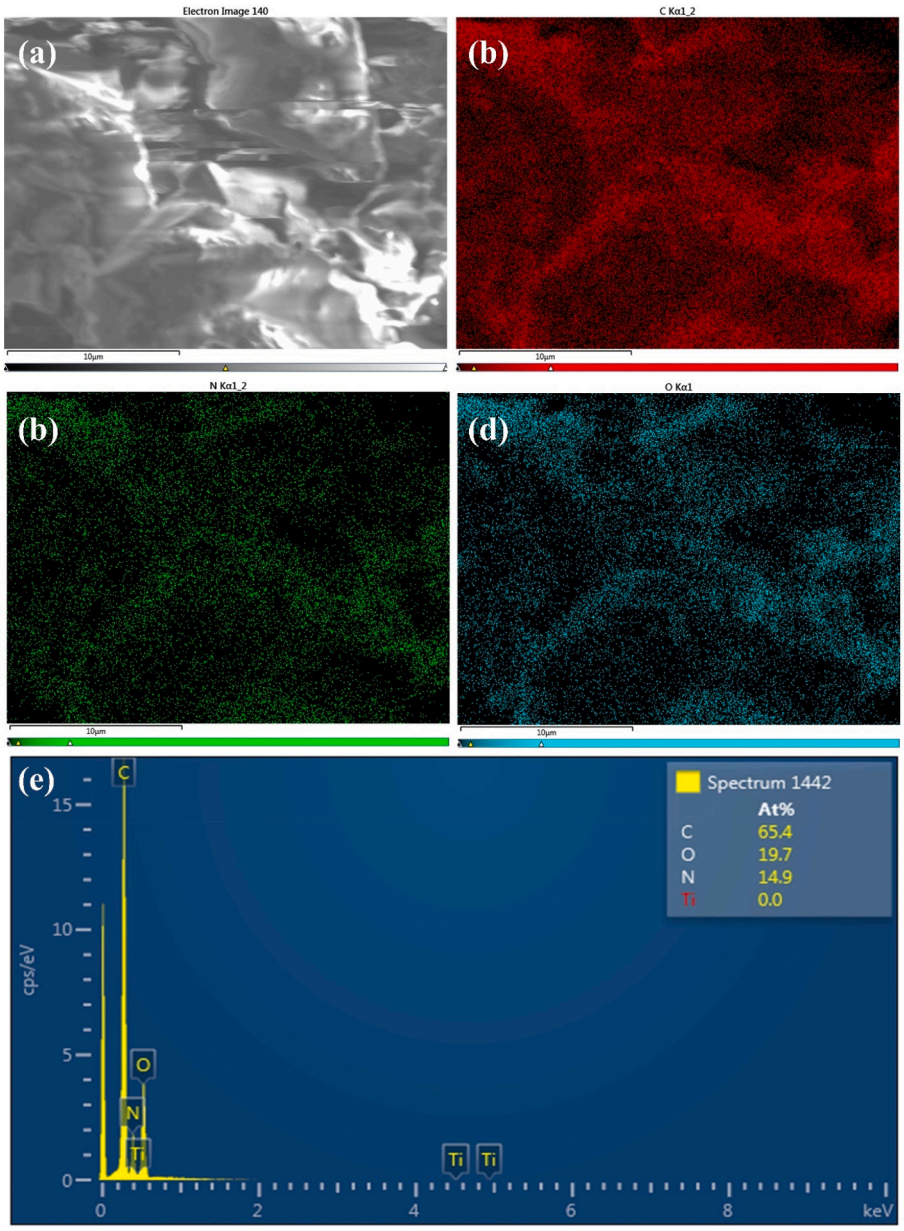

Fig. 5. (a) SEM image of C-dot, EDX mapping of (b) C, (c) N, and (d) O in C-dot, and (e) elemental analysis report of C-dot nanoparticle from SEM-EDX analysis.

observed, the XRD spectrum of MXene nanoparticles shows a good match with that of Ti_3AlC_2 (JCPDS 52–0875 (Gou et al., 2021; Sengupta et al., 2020)). The characteristics peaks were observed at 2θ angles of 8.8°, 18.16°, and 60.7°, which corresponds to the (002), (006), (008), and (110) crystallographic planes, respectively. The XRD spectrum for carbon dot nanoparticles shows a main peak at 2 θ angle of 18.56°, which corresponds to crystallographic plane (002) of carbon (JCPDS 26–1076) (Shaikh et al., 2018). The broad peak confirms the fluorescence property and considerably very small crystallite size distributions of the synthesized C-dot nanomaterials, and was consistent with previous reports from literature (Rub Pakkath et al., 2018; Sun et al., 2016). As observed from the XRD spectrum of hybrid MXene/C-dot nanomaterial, all the peaks from the crystalline MXene nanosheet are present. However, a shift in the peaks corresponding to planes (002), (006), (008), and (110) was observed. The characteristic peak of (002) at 8.7° was shifted to the left to 6.92°. The peak shifting could be to increase the MXene layer spacing to accommodate the C-dot nanoparticles. This observation was in accordance with previously reported characterization studies from literature on MXene nanocomposite (Feng et al., 2022). The (006), and (110) planes shifted to right from 18.16 to 20°, and 60.7 to 61.1°, respectively. This could be arising due to the probe sonication and the microwave heat treatment conducted during the synthesis (Zhang and Zhang, 2022).

3.4. Raman spectroscopic analysis

As observed from Fig. 9, the C-dot is showing a broad peak indicating the luminescence property of the C-dot. The G-band due to the in-plane C–C deformation (Dervishi et al., 2019) was observed at 1599.4 cm^{-1}, which corresponds to the sp2 hybridized carbon atoms (Edison et al., 2016). And the peak at 1359 cm^{-1} indicates the D-band of the C-dot nanoparticle which indicates the sp3 defects in the carbon atom. The D-band is caused due to the vibrations of carbon atoms with dangling bonds in the termination plane of disordered graphite. The intensity ratio of D and G-band (ID/IG) was 0.79. ID/IG value being less than one indicates that the as-synthesized carbon is heavily graphitized (Edison et al., 2016; John et al., 2022). Hence, the Raman spectroscopic analysis shows that the as-prepared C-dot have a graphitic structure consisting of

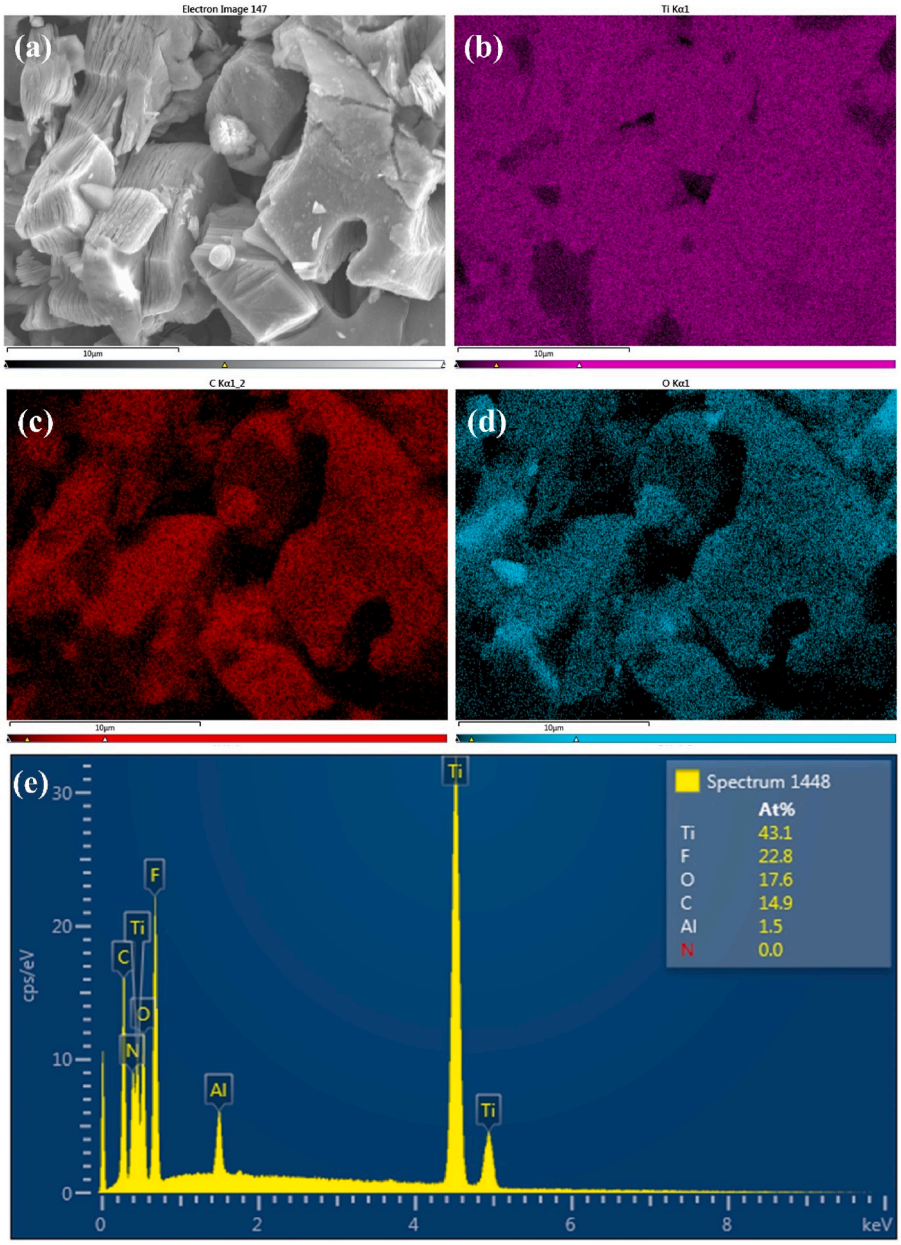

Fig. 6. (a) SEM image of MXene, EDX mapping of (b) Ti, (c) C, and (d) O in MXene, and (e) elemental analysis report of MXene nanosheet from SEM-EDX analysis.

hybridized sp2 carbon atoms and defected sp3 carbons. The Raman spectrum of MXene shows two distinct peaks at 1355 and 1601 cm^{-1} which represent the D-band and G-band, respectively. The D-band is associated with the disordered graphite structure and defects. While the G-band corresponds to the signal from graphite (Li et al., 2017). The intensity of D and G peaks was calculated to be about 0.84. The spectrum also shows peaks at 391.44, 519.64, and 642.27 cm^{-1}. These peaks could be attributed to the vibrational modes of B1g (1), A1g & B1g (2), and Eg (3), respectively (Naguib et al., 2014; Swamy et al., 2005), which are also indicative of MXene (Hu et al., 2015; Wen et al., 2019). The absence of peaks from aluminium (185, 201 and 272 cm^{-1}) indicates that the Al was etched completely and no trace elements are present (Wang et al., 2016). The Raman spectrum of MXene/C-dot nanoparticle shows D and G bands at 1356.6 and 1595.4 cm^{-1}. In comparison to MXene, the fluorescence property of the carbon dot is visible from the Raman spectrum of the hybrid nanoparticle. The intensity of peaks due to anatase vibrational modes is reduced due to the fluorescence intensity caused by carbon dots. A redshift in the D-band by about 10 cm^{-1} was observed, which could be attributed to the defects occurring due to the high-temperature microwave synthesis method. This could also be occurring due to the interaction between MXene and C-dot nanoparticles in the hybrid material (Wen et al., 2019). The ID/IG ratio has also increased to 0.85 in comparison to 0.79 for pure MXene. This also confirms the increase in defects in MXene after the introduction of the C-dot (Wen et al., 2019).

3.5. Elemental compositional analysis

The XPS spectrum of all three samples is displayed in Fig. 10, Fig. 11, and Fig. 12. The survey spectrum of C-dot as observed in Fig. 10 (a), shows the presence of three main elements C, O, and N with compositions of 67.78, 20.63, and 10.72 %, respectively. The C 1s deconvolution spectrum of C-dot as observed from Fig. 10 (b) shows four peaks at BE values of 284.67, 286.09, 287.9, and 288.65 eV, corresponding to the functional groups of C–C, C–N, C = 0, and O–C═O, respectively. The peaks observed at the respective BE values were found to be agreeing

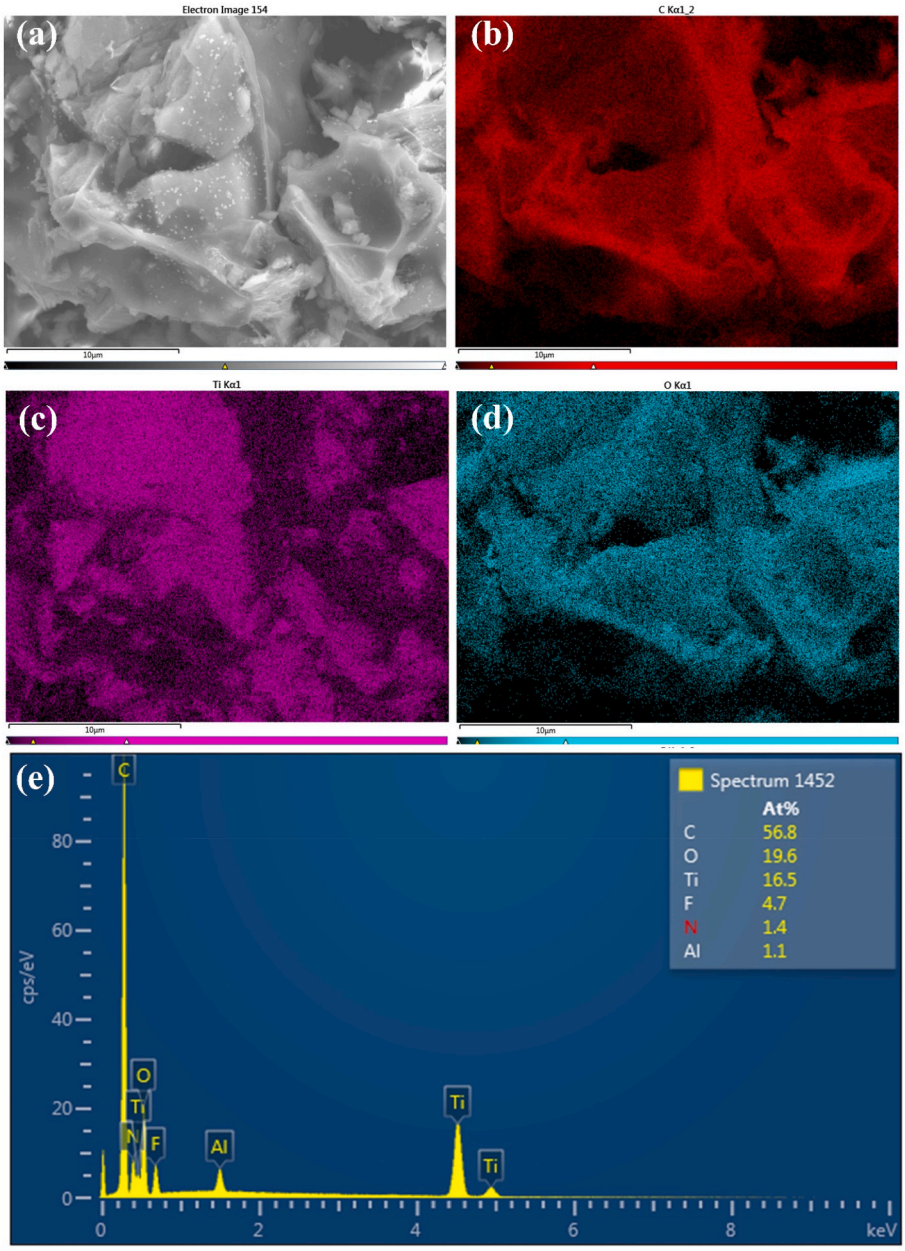

Fig. 7. (a) SEM image of MXene/C-dot, EDX mapping of (b) C, (c) Ti, and (d) O in MXene/C-dot, and (e) elemental analysis report of MXene/C-dot from SEM-EDX analysis.

with the literature (Niu et al., 2015).

The survey spectrum of MXene nanomaterial as shown in Fig. 11 (a) confirms the presence of four major elements namely, titanium (Ti), carbon (C), and oxygen (O) of atomic weight percentage by 61.49, 21.99, and 8.46 %, respectively. Fluorine was detected due to the usage of hydrogen fluoride during the etching of aluminium layers from Ti_3AlC_2 to obtain MXene nanosheets. The Ti 2p spectrum of MXene shows peaks at 454.4, 455.62, 459.16, 460.8, 462, and 464.82 eV. The Ti–C bond was observed at 454.4eV. Ti2+ 2p3/2 and Ti2+ 2p1/2 were detected at binding energies of 455.62 and 460.8 eV, respectively. Peaks at 459.16 and 462 eV correspond to Ti3+ and Ti4+. The peak at 464.82 eV could be due to Ti–F bonds. The Ti 2p spectrum resembled that of the previously reported works in literature (Cao et al., 2017; Krishnamoorthy et al., 2017). The C 1s spectrum shows two major peaks at BE values of 280.67, and 283.63 eV, which confirms the presence of C–Ti and C–C bonds, respectively. Other peaks occur at binding energies of 281.28, 284.48, and 287.87 eV, corresponding to functional groups of C–Ti–O, C═O, and C–F, respectively (Du et al., 2019; Sun et al., 2016). The presence of fluorine is indicated by the F 1s spectrum as it shows two peaks corresponding to Ti–F and F–C at binding energies of 684 and 685.72 eV, respectively (Li et al., 2019). The O 1s spectrum shows the presence of TiO2, C–Ti-Ox, C–Ti-OHx, and water molecules at BE values of 529.2, 530, 531.25, and 532.9 eV respectively.

The Ti 2p spectrum of hybrid MXene/C-dot as observed in Fig. 12 shows 7 peaks at 455.1, 456.48, 458, 459.1, 460.94, 462.61, and 464.61 eV. The Ti–C 2p1/2 and 2p3/2 bonds were detected at 455.1 and 460.94 eV (Li et al., 2020; Wang et al., 2018). As indicated by the Ti–O 2p1/2, and 2p3/2 bonds, titanium was bonded with oxygen after being oxidised during the microwave pyrolysis process during hybrid material synthesis. The peaks from C 1s show the carbon bonds C–Ti, C–O, C–C, C═O, and O–C═O at binding energies of 280.85, 284.08, 285.01, 287.43, and 288.47 eV, respectively. The C–C bond was observed to be having the highest peak intensity, followed by the C═O bond. The Ti–C bond was observed to be having the least intensity. Trace fluorine

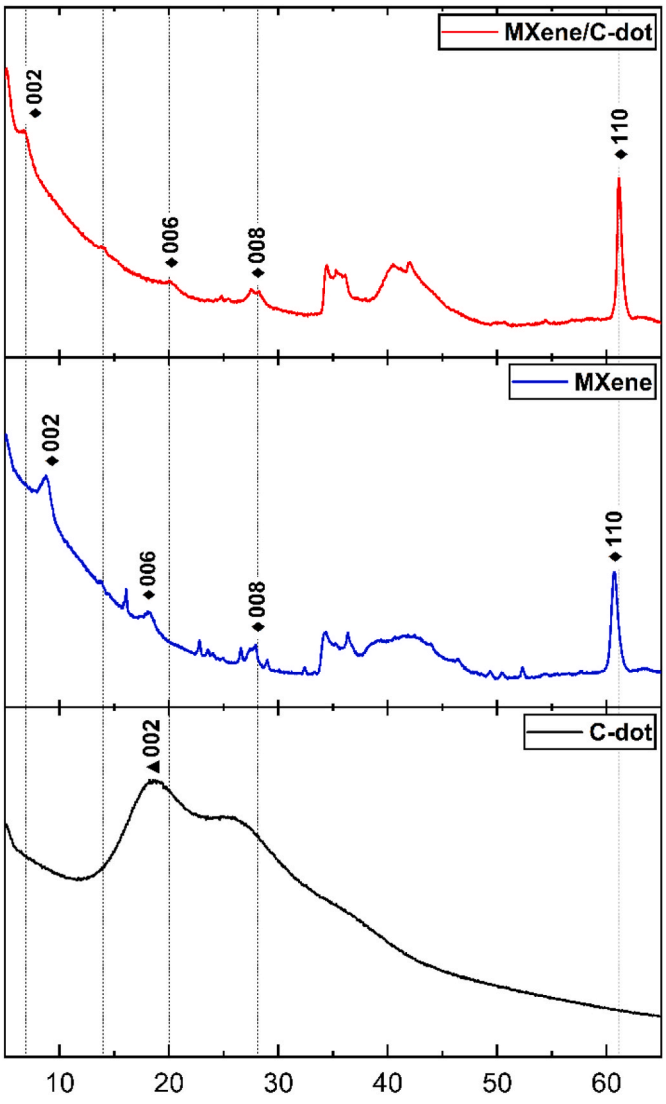

Fig. 8. XRD spectrum of C-dot, MXene, and MXene/C-dot nanofluid.

element from MXene was observed to show bonding with titanium and carbon after the synthesis process to form Ti–F and Fi-C bonds and was detected in the F 1s spectrum at BE of 684.15 and 685.57 eV, respectively. The change in BE for the doublet splitting of Ti (IV) 2p1/2–3/2 splitting was about 5.64 (Reference was 5.66 for Ti (IV) (Biesinger et al., 2010)). The XPS survey spectrum of hybrid nanoparticles, shown in Fig. 12 (a), in comparison to MXene, shows that an additional N 1s peak with high intensity was observed at 401.98 eV. This additional peak could be attributed to the hybridization of C-dot on the MXene surface (Geng et al., 2021). The elemental composition of hybrid nanomaterial is contributed mainly by C, O, N, and Ti by 60.20, 20.33, 9.31, and 8.18 %, respectively.

3.6. Thermal property analysis

Understanding the thermal characteristics of HTFs are necessary to assess their feasibility in suitable heat transfer applications. Thermal conductivity and volumetric heat capacity of the nanofluids are explained in this section.

3.6.1. Thermal conductivity analysis

Variations of thermal conductivity of nanofluid with temperature and the corresponding enhancement over base fluid could be observed

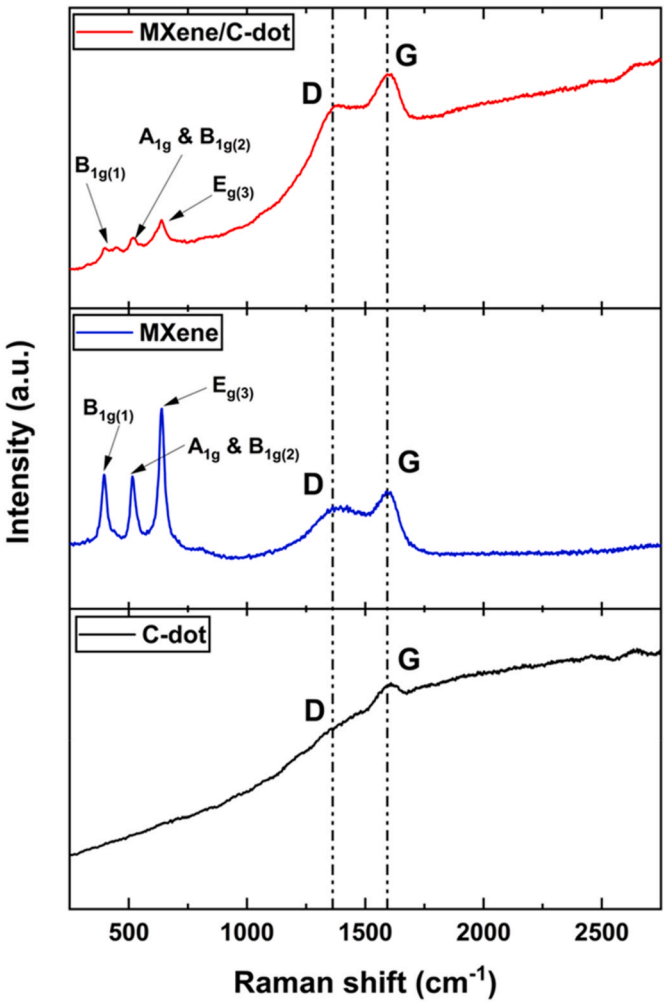

Fig. 9. Raman spectrum of C-dot, MXene, and MXene/C-dot nanofluid.

in Fig. 13 (a), (c), and (e). As inferred from the thermal conductivity plot of the C-dot in Fig. 13 (a), the thermal conductivity of nanofluid increased with an increase in the concentration of nanofluid. This increase is predominantly caused due to high thermal conductivity of the nanomaterial in comparison to base fluid. The difference in thermal conductivity between 0.01 wt % and 0.05 wt % was observed to be minimal. However, a significant increase was noticed in the thermal conductivity of nanofluid value with an increase in the concentration beyond 0.05 wt %. Also, the curve of TC was observed to rise steeper with an increase in fluid temperature beyond 30 °C. Brownian motion and thermophoretic effect are the two underlying phenomenon that enhances the thermal conductivity of nanofluid with temperature (Godson et al., 2010). The highest thermal conductivity was found to be 0.885 $Wm^{-1}K^{-1}$ at a fluid temperature of 60 °C. Enhancement in the TC value of C-dot over base fluid is plotted in Fig. 13 (b). Thermal conductivity enhancement of C-dot over DI water was highest at 60 °C for all concentrations. The corresponding increment was from 19.66 to 33.21 % with an increase in concentration of C-dot from 0.01 to 0.2 wt %. The thermal conductivity of MXene nanofluid and the corresponding graph of enhancement over DI water are depicted in Fig. 13 (c) and (d), respectively. Compared to C-dot, the variation of TC with temperature is more linear. The results indicate that MXene nanofluid has significant thermal conductivity. The value increased from 0.628 to 0.828 $Wm^{-1}K^{-1}$ for 0.01 wt %. The highest thermal conductivity of about 1.003 $Wm^{-1}K^{-1}$ was reported for 0.2 wt % at 60 °C. As observed from Fig. 13 (d), the highest enhancement of 50 % was also reported at this point. Similarly, Fig. 13 (e) and (f) visualize the thermal conductivity

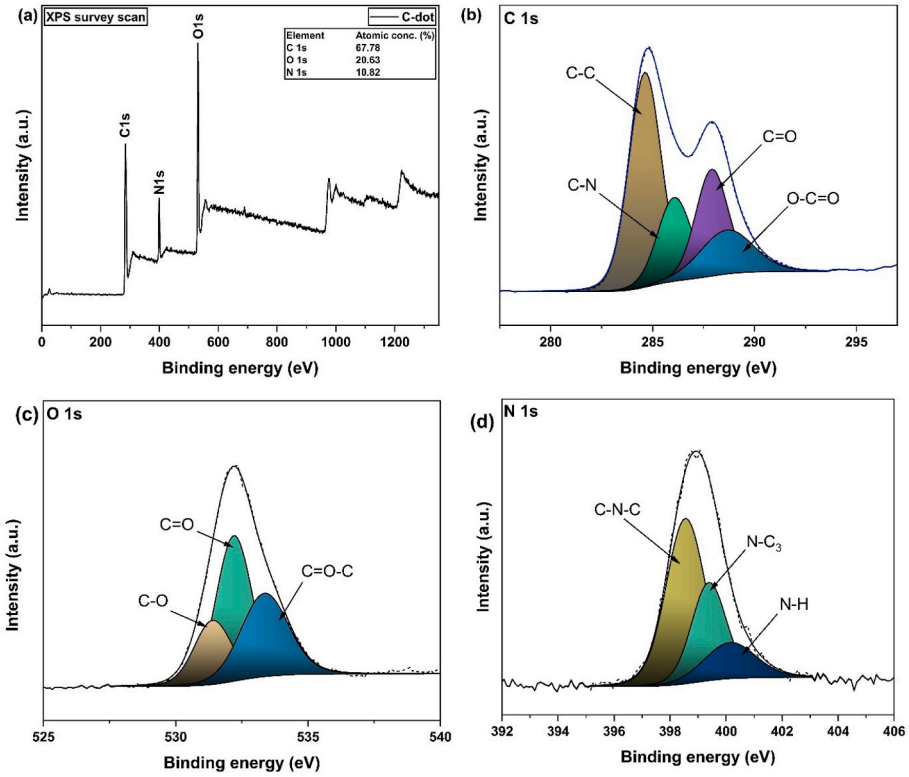

Fig. 10. XPS analysis of C-dot showing (a) survey (b) C 1s, (c) O 1s, and (d) N 1s spectrums.

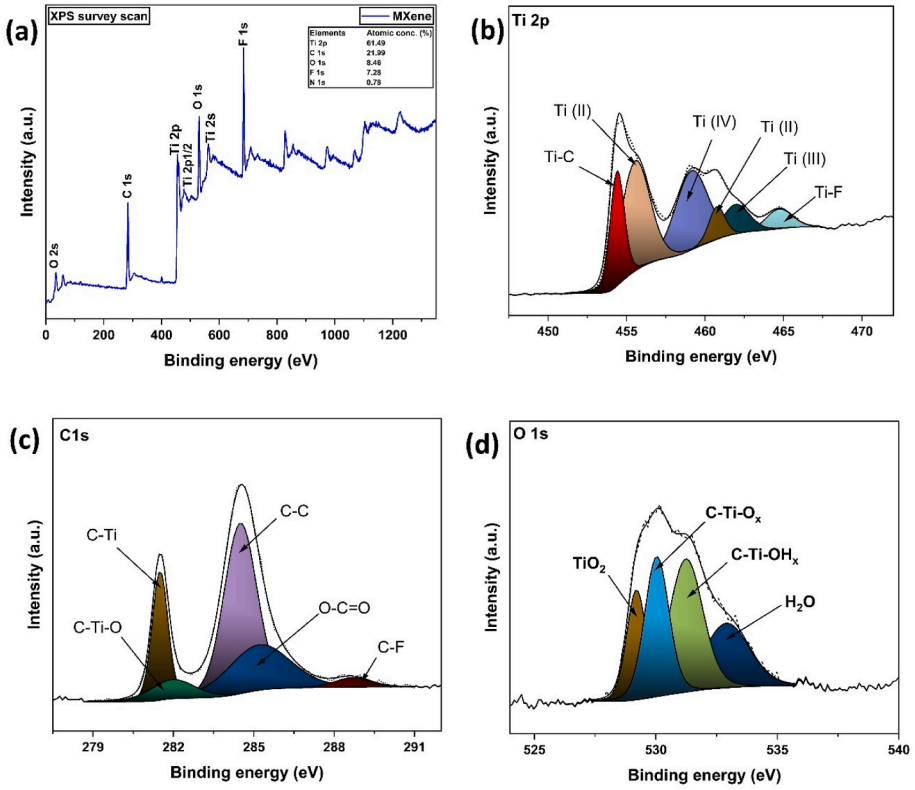

Fig. 11. XPS analysis of MXene showing (a) C1s spectrum, (b) Ti2p spectrum, (c) O1s spectrum and (d) survey.

variation of hybrid nanofluid with measurement temperature and the corresponding increment in comparison to that of DI water. The result shows that the thermal conductivity of the hybrid is higher than that of the C-dot nanofluid due to the introduction of MXene nanomaterial. The highest observed thermal conductivity varied from 0.810 to 0.945 $Wm^{-1}K^{-1}$ for 0.01 and 0.2 wt % nanofluids, respectively. About 42.2 %

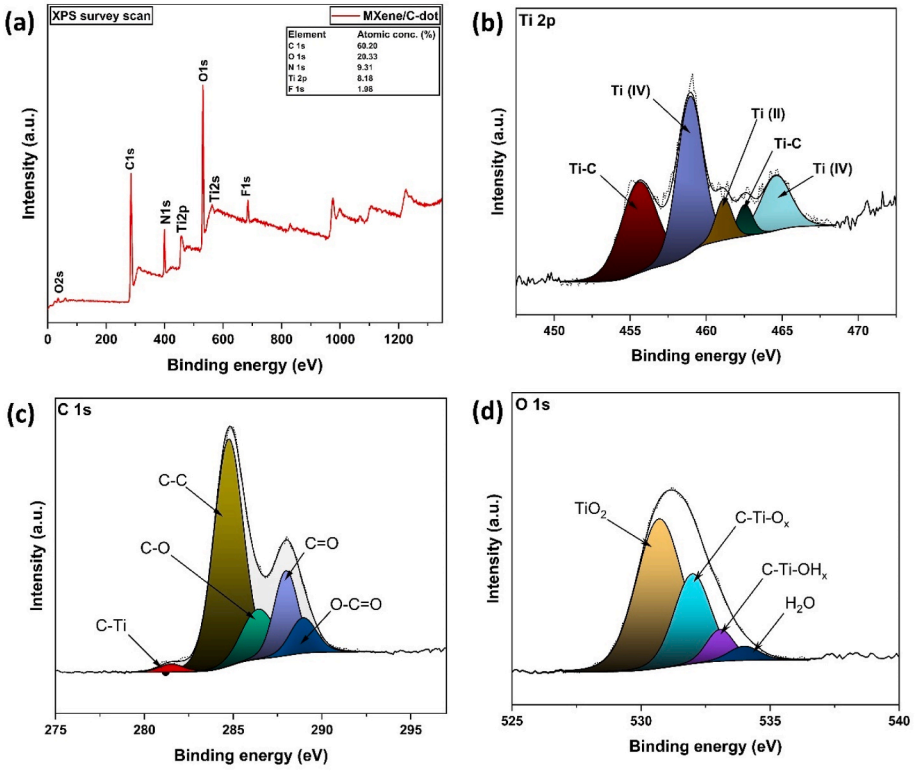

Fig. 12. XPS analysis of MXene/C-dot showing (a) C1s spectrum, (b) Ti2p spectrum, (c) O1s spectrum and (d) survey.

enhancement was calculated for the hybrid over base fluid. The findings suggest that MXene exhibits the highest thermal conductivity in comparison to C-dot and base fluid. However, the hybrid nanofluid is showing comparable thermal conductivity as MXene due to the synergistic effect of C-dot and MXene in the medium.

A semi-empirical correlation was coined to predict the thermal conductivity of nanofluid, as a function of nanofluid concentration and temperature. Analysis of variance (ANOVA) study was performed using the software Design-Expert® 11 to understand the interaction effect of fluid temperature and concentration on the thermal conductivity of fluids. The details on the methodology adopted for this analysis and the interaction effects are shown in **Section S4** of the Supplementary data file. Equations (8)–(10), are used to predict the thermal conductivity of C-dot, MXene and hybrid nanofluid, respectively. The developed correlation agreed well with the experimentally recorded data with an R^2 value of 0.9964, 0.9931, and 0.9901 for C-dot, MXene, MXene/C-dot nanofluids, respectively.

$$k_{TC,C-dot} = 0.562681 + 0.226675.\varphi_{C-dot} + 6.03\times10^{-4}.T_{C-dot} + 6.79\times10^{-4}.\varphi_{C-dot}.T_{C-dot} - 2.33098.\varphi^2_{C-dot} + 5.7\times10^{-5}.T^2_{C-dot} + 8.9953\times10^{-5}.\varphi^2_{C-dot}.T^2_{C-dot} \quad (8)$$

$$k_{TC,MXene} = 0.643073 - 0.72344.\varphi_{MXene} - 3.248\times10^{-3}.T_{MXene} + 2.171\times10^{-2}.\varphi_{MXene}.T_{MXene} + 1.6371.\varphi^2_{MXene} + 1.02\times10^{-4}.T^2_{MXene} \quad (9)$$

$$k_{TC,MXene/C-dot} = 0.531369 - 0.62041.\varphi_{MXene\ /\ C-dot} + 3.022\times10^{-3}.T_{MXene\ /\ C-dot} + 4.3135\times10^{-2}.\varphi_{MXene\ /\ C-dot}.T_{MXene\ /\ C-dot} + 6.49325.\varphi^2_{MXene\ /\ C-dot} + 1.5\times10^{-5}.T^2_{MXene\ /\ C-dot} - 0.424877.\varphi^2_{MXene\ /\ C-dot}.T_{MXene\ /\ C-dot} - 5.17.\times10^{-4}.\varphi_{MXene\ /\ C-dot}.T^2_{MXene\ /\ C-dot} + 7.038\times10^{-3}.\varphi^2_{MXene\ /\ C-dot}.T^2_{MXene\ /\ C-dot} \quad (10)$$

3.6.2. Volumetric heat capacity analysis

Thermal conductivity and thermal diffusivity values were used to calculate volumetric heat capacity as shown in Equation (1). The thermal diffusivity value of base fluid and nanofluids at each concentration and temperature are shown in the Supplementary data file (Section S3). Variation of volumetric heat capacity of nanofluids with temperature is depicted in Fig. 14 (a) – (c). The heat capacity was observed to decrease with an increase in temperature and concentration of the nanofluid. The highest volumetric heat capacity of all the nanofluids was almost the same around 4.12 $MJm^{-3}K^{-1}$ and was measured at a fluid temperature of 20 °C and 0.01 wt %. The volumetric heat capacity of the hybrid nanofluid decreased by about 0.47 $MJm^{-3}K^{-1}$ with an increase in fluid temperature by 40 °C. The variation of volumetric heat capacity was in accordance with previously reported studies in literature (Zhou and Ni, 2008). The decrease in the specific heat of nanofluid with an increase in nanoparticle concentration could be attributed to the lower specific heat value of nanomaterial in comparison to base fluid (Mousavi et al., 2019; Shahrul et al., 2014). Another reason is the solid-liquid interfacial free energy change occurring with the addition of nanoparticles (Wang et al., 2006). With a larger surface area of nanoparticles, higher will be the effect of surface free energy on the heat capacity of the fluid. Hence, careful selection of base fluid, nanomaterial, and concentration is required to improve the specific heat of nanofluid.

The semi-empirical formulae for predicting the volumetric heat capacity of nanofluids were correlated. The details on the ANOVA analysis models used for generating the correlations are shown in **Section S5** of the Supplementary data file. The regression model was agreeing with the experimental data with R^2 values of 0.9931, 0.9917, and 0.9952 for C-dot, MXene, and MXene/C-dot nanofluids, respectively. The volumetric heat capacity of C-dot, MXene and hybrid nanofluid, at a specific concentration and temperature, could be calculated using Equations (11)–(13), respectively.

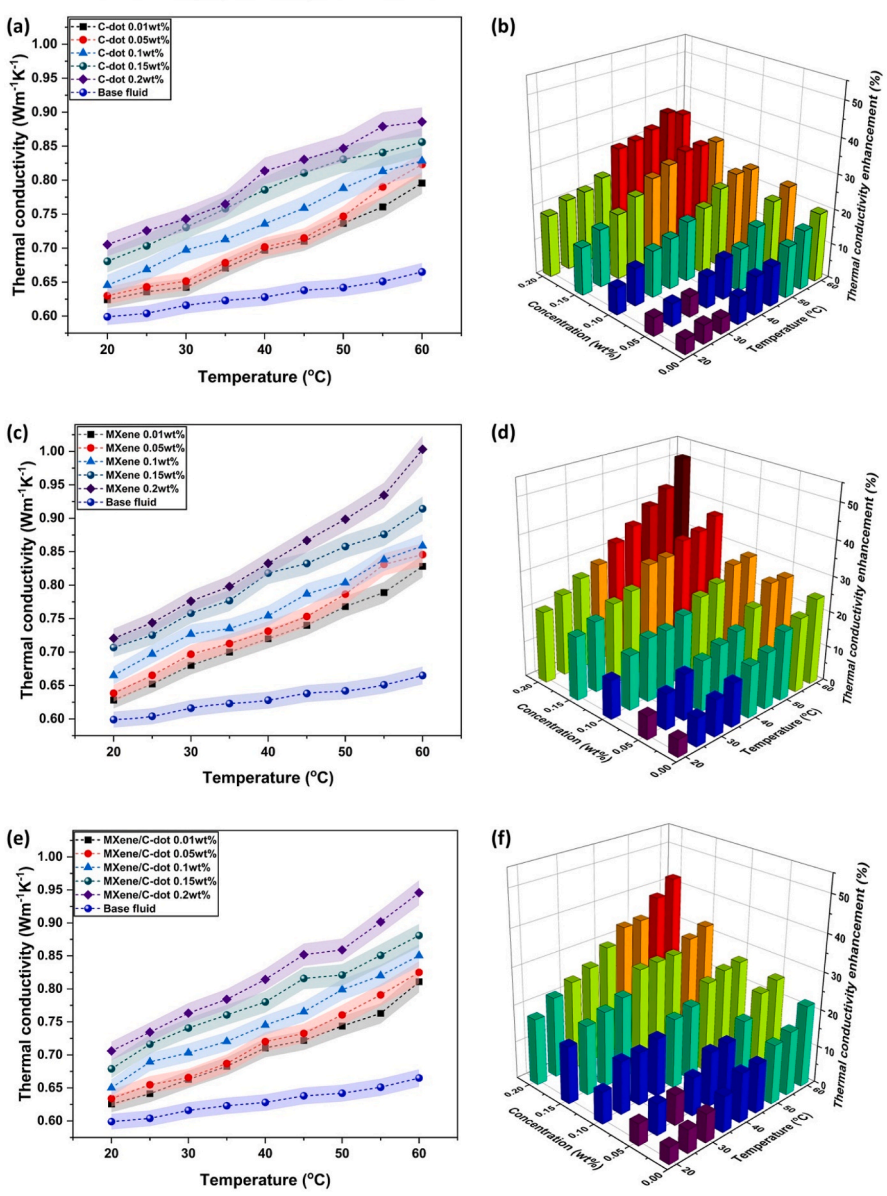

Fig. 13. Temperature-dependent variation of thermal conductivity of (a) C-dot, (c) MXene, and (e) MXene/Cdot nanofluids and base fluid; and thermal conductivity enhancement of (b) C-dot, (d) MXene, and (f) MXene/Cdot nanofluids over base fluid.

$$C_{p\ vol,C-dot} = 4.43507 - 3.04725.\varphi_{C-dot} - 0.013347.T_{C-dot} + 0.029742.\varphi_{C-dot}.T_{C-dot} + 0.821018.\varphi^2_{C-dot} + 5.17835\times10^{-6}.T^2_{C-dot} \quad (11)$$

$$C_{p\ vol,MXene} = 4.36802 - 2.47081.\varphi_{MXene} - 0.010889.T_{MXene} + 0.024493.\varphi_{MXene}.T_{MXene} - 0.178182.\varphi^2_{MXene} - 4.73506 \times 10^{-6}.T^2_{MXene} \quad (12)$$

$$C_{p\ vol,hybrid} = 4.41316 - 2.8528.\varphi_{hybrid} - 0.012557.T_{hybrid} + 0.027889.\varphi_{hybrid}.T_{hybrid} + 0.500732.\varphi^2_{hybrid} + 2.31152 \times 10^{-6}.T^2_{hybrid} \quad (13)$$

3.7. Optical property analysis

Transmittance of C-dot, MXene and MXene/C-dot nanofluids are shown in Fig. 15 (a), (b), and (c), respectively. As observed from Fig. 15 (a), all concentrations of C-dot nanofluid show high transmittance in the spectral range of 930–2000 nm and resemble that of the base fluid. The spectrum below 930 nm shows that the transmittance of the nanofluids decreases with an increase in concentration. In this region, the transmittance of all the fluids falls steeply till 330 nm. A peak in transmittance was observed only in the case of C-dot with lower concentrations (0.01 and 0.05 wt %). As observed, the highest transmittance corresponds to 0.01 wt % C-dot and the least pertains to 0.2 wt %. Transmittance spectra of MXene nanofluids as seen in Fig. 15 (b) show that the transmittance was decreasing steadily along the spectrum with the increase in concentration. The transmittance of the nanofluids and base fluid is almost the same above 1400 nm. As observed from the graph, the decrease in transmittance with concentration is predominant for concentrations below 0.1 wt %. The decrement in transmittance with an increase in concentration above 0.1 wt %, is comparatively less. The spectral transmittance of MXene/C-dot hybrid nanofluid is shown in Fig. 15 (c). As observed, the transmittance spectra of the fluid are a blend of transmittance characteristics of both MXene and C-dot nanofluid. The steep decrease in transmittance below 600 nm wavelength, and a small peak in transmittance around 300 nm are the characteristics

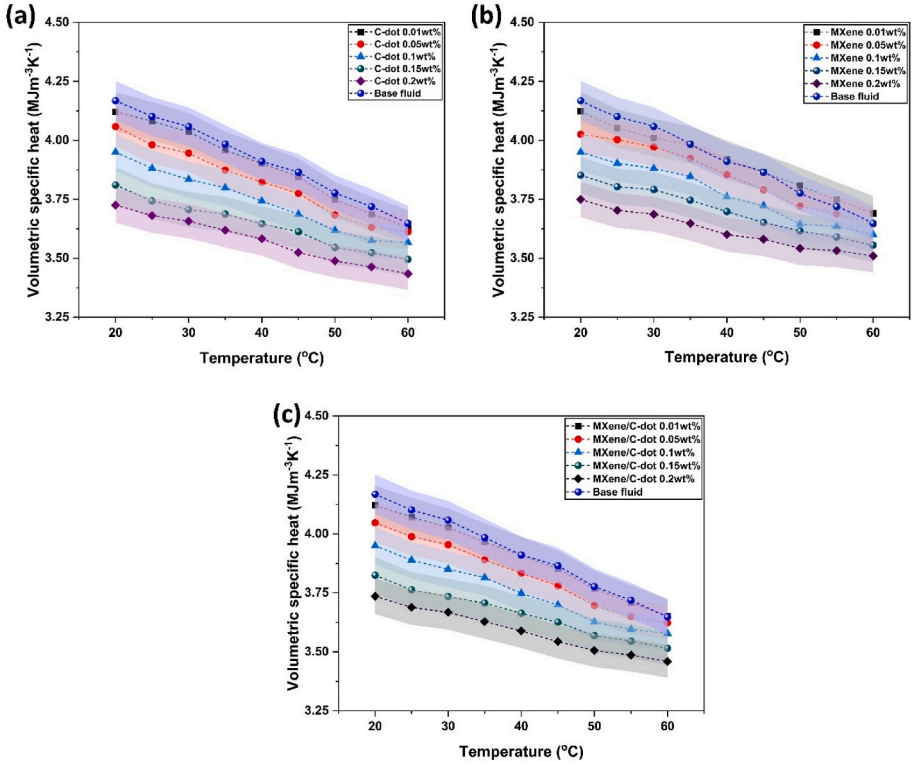

Fig. 14. Temperature-dependent variation of volumetric heat capacity of (a) C-dot, (b) MXene, and (c) MXene/C-dot nanofluids.

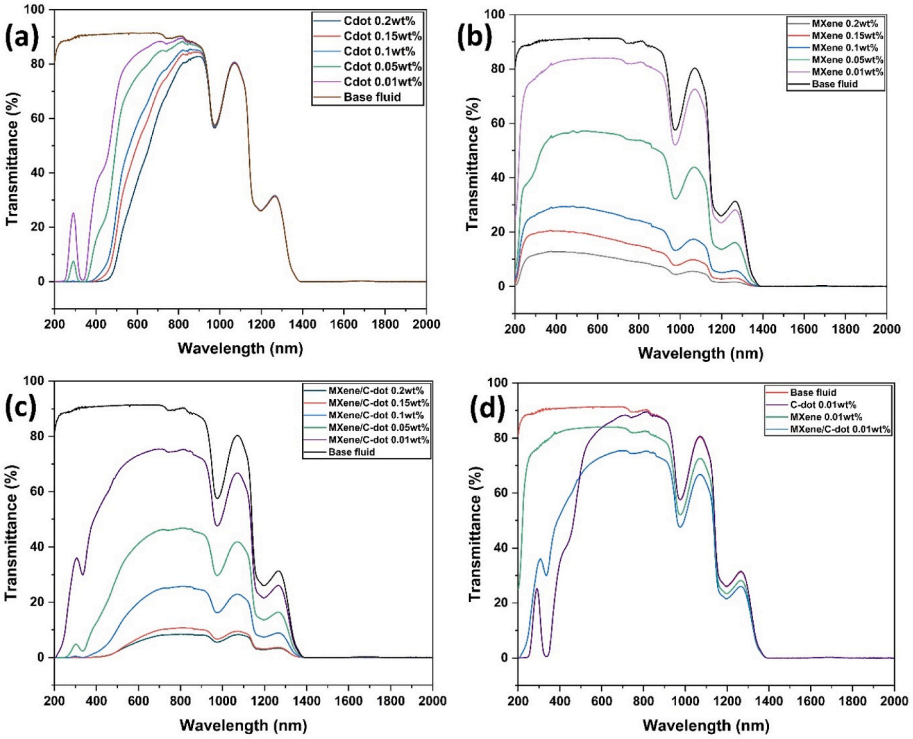

Fig. 15. Transmittance spectra of nanofluids (a) C-dot, (b) MXene, (c) MXene/C-dot nanofluid, and (d) all the nanofluids of 0.01 wt%, and base fluid.

of C-dot nanofluid. The transmittance curve of the C-dot nanofluid was almost similar to that of base fluid above 930 nm. The hybrid nanofluid shows a considerable decrease in transmittance in the range 930–1400 nm which could be attributed to the optical absorptivity of MXene nanofluid.

Spectral absorption and scattering coefficients of the nanofluids and base fluid were calculated and visualized as shown in Fig. 16 (a) – (f). The absorption spectrum of C-dot nanofluid as observed in Fig. 16 (a), indicates that increasing the concentration can enhance the absorption coefficient of fluid. C-dot of 0.2 wt % was found to be showing higher

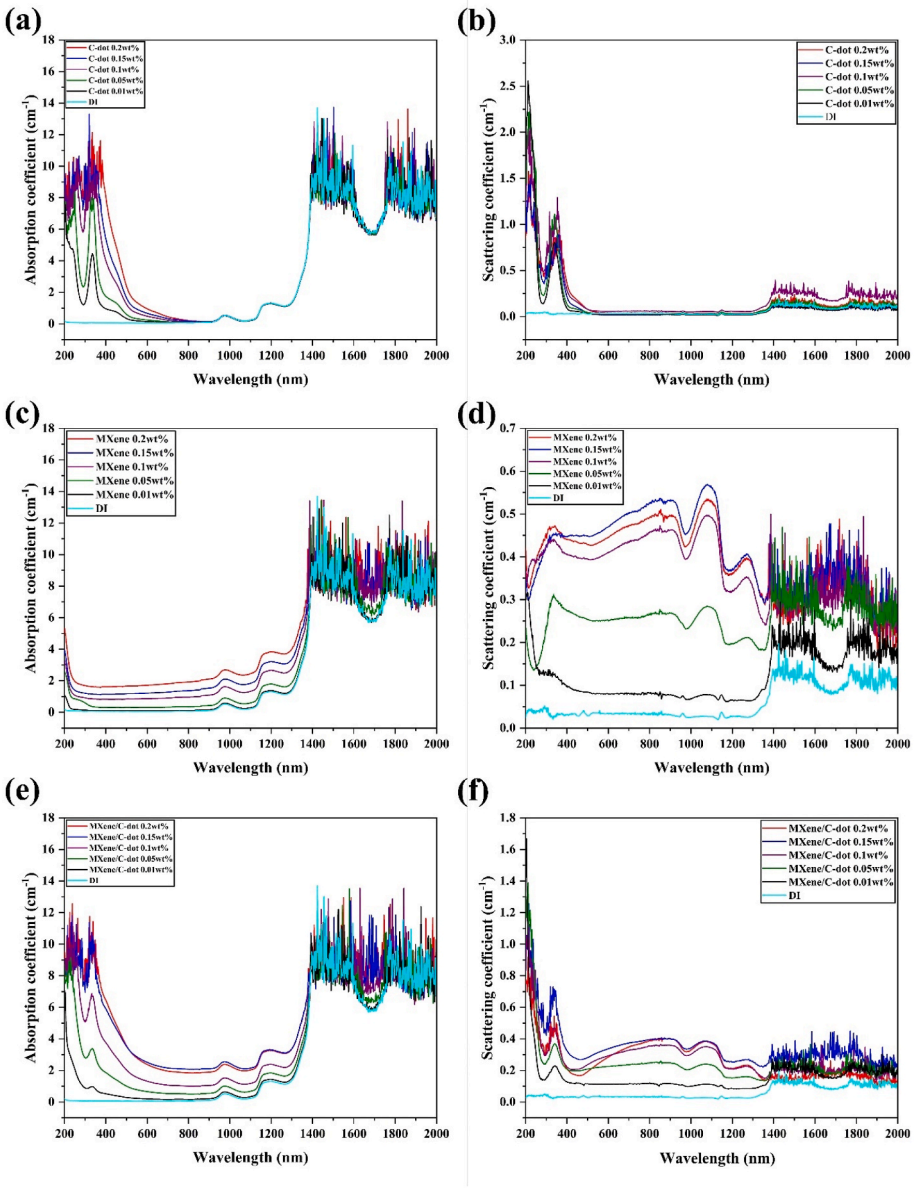

Fig. 16. Spectral absorption coefficient of (a) C-dot, (c) MXene, and (e) MXene/C-dot nanofluid; and spectral scattering coefficient of (b) C-dot, (d) MXene, and (f) MXene/C-dot nanofluid.

absorption in comparison to other concentrations throughout the spectrum. The beam radiation was highly absorbed in the wavelength between 200 and 800 nm. The scattering coefficient depicted in Fig. 16 (b) shows that the variation was nonlinearly dependent on the concentration. The scattering coefficient peaked for a C-dot of 0.01 wt % at 215 nm. The scattering coefficient peak was found to decrease with the increase in the concentration of C-dot at this range of 200–300 nm. In the wavelength range of 300–2000 nm, a C-dot of 0.1 wt % was found to be showing a higher scattering coefficient, followed by 0.2, and 0.05 wt %. C-dot of 0.15 and 0.01 wt % were observed to be showing the least scattering in comparison to other nanofluids. It is worth noticing that the amount of light scattered in the C-dot of 0.15 and 0.01 wt % was comparatively lower than that of DI water. This indicates that the C-dot of 0.15 wt % having a higher absorption coefficient and lower scattering coefficient is a better candidate for photothermal applications. The absorption spectrum of MXene nanofluid in Fig. 16 (c) shows that the absorption coefficient increases with nanofluid concentration. The increment in absorption coefficient was predominant in the range of 200–1300 nm. The scattering coefficient as observed in Fig. 16 (d) shows that the light was more scattered while passing through 0.15 wt % MXene. The 0.2 wt % nanofluid showed the second-highest scattering coefficient along the spectrum. The absorption spectrum of hybrid nanofluid as depicted in Fig. 16 (e), reveals that MXene/C-dot of 0.15 and 0.2 wt % could absorb more radiation as their absorption curves were almost coinciding across the spectral range. Comparing the absorption coefficient spectrum of hybrid with other nanofluids, a synergistic enhancement in radiation absorption was observed. C-dot had peak absorption along 200–800 nm and after 800 nm the absorption coincided with that of the base fluid. And MXene was showing steady absorption in the range of 200–1380 nm. Hence, in the case of hybrid, an intrinsic absorption coefficient peak of C-dot was observed within 200–600 nm. A steady increment was noticed till 1380 nm, which is due to the absorption of MXene. The corresponding synergistic pattern could be observed in the scattering coefficient plot of the hybrid nanofluid in Fig. 16 (f). The characteristic scattering coefficient peaks of C-dot (along 200–400 nm) and MXene (along 600 to 1200 nm) were observed for the hybrid nanofluid.

4. Conclusions

A novel MXene/C-dot hybrid nanofluid having synergistic properties of individual nanofluids was developed using a cleaner and less energy-intensive in-microwave synthesis route. The study performs morphological, phase structure, and chemical compositional analysis on the hybrid nanomaterial. The thermal conductivity, volumetric heat capacity, and optical absorptivity properties of the hybrid nanofluid and individual nanofluids were analysed in the study. The major findings from the study include:

- The morphological analysis observed multilayered nanosheets for MXene, and delaminated MXene nanosheets with carbon dot deposition in the case of hybrid nanocomposite.
- XRD analysis shows that C-dot exhibits crystalline phase structure. The phase structure of hybrid nanomaterial exhibited a shift due to the synthesis process. The fluorescence characteristic of the carbon dot is discernible from the hybrid nanoparticle's Raman spectrum in comparison to the MXene nanoparticle.
- Compared to 0.79 for pure MXene, the ID/IG ratio has increased to 0.85 for hybrid nanomaterial. This further supports the finding that MXene defects increased with the introduction of C-dot.
- XPS spectroscopy shows that additional chemical bonds were created in the Ti 2p spectrum of hybrid nanoparticles in comparison to MXene. Hence, each analysis has helped to confirm the hybridization of MXene and C-dot in the hybrid nanomaterial.
- Semi-empirical correlations were coined to predict the thermal conductivity and volumetric specific heat of nanofluids at a specific concentration and temperature. Effective thermal property prediction makes the design of nanofluid based energy systems easier, and energy-efficient. The proposed correlations are limited to the thermal property prediction of MXene, C-dot, and MXene/C-dot nanofluids.
- Thermal conductivity was observed to increase with concentration and fluid temperature. MXene nanofluid showed the highest thermal conductivity of 1.003 $Wm^{-1}K^{-1}$ at 0.2 wt % which was an enhancement of 50 % over base fluid. Hybrid and C-dot nanofluids were observed to have enhancement of 42.2 and 33.2 %, respectively.
- Volumetric heat capacity decreased with an increase in nanofluid concentration and temperature. Volumetric heat capacity reached a maximum of around 4.12 $MJm^{-3}K^{-1}$ for all the nanofluids at the lowest concentration of 0.01 wt %.
- Transmittance spectra of hybrid nanofluid were observed to have the characteristics of the component nanomaterials. This complimentary property was also observed in the absorption and scattering coefficient spectrums.
  •The scattering coefficient of 0.15 wt % C-dot was found to be lower than that of the base fluid. The absorption coefficient was almost as high as 0.2 wt % C-dot, hence making 0.15 wt % C-dot better suited for optical solar applications. Similarly, 0.1 wt % MXene showed better optical properties suited for solar applications. And hybrid nanofluid of 0.15 wt % exhibited a high absorption coefficient in comparison to other concentrations.

The study presents that MXene and MXene/C-dot nanofluids have exceptional thermal, and optical properties. These characteristics make them desirable for heat transfer applications as a cleaner, and an energy efficient choice.

CRediT authorship contribution statement

Sreehari Sreekumar: Writing – original draft, Visualization, Validation, Methodology, Investigation, Formal analysis, Data curation, Conceptualization. **Abhijit Ganguly:** Writing – review & editing, Visualization, Validation, Investigation, Formal analysis. **Sameh Khalil:** Investigation, Formal analysis. **Supriya Chakrabarti:** Writing – review & editing, Supervision, Resources, Conceptualization. **Neil Hewitt:** Supervision, Resources, Project administration, Conceptualization. **Jayanta Deb Mondol:** Writing – review & editing, Supervision, Resources, Project administration, Conceptualization. **Nikhilkumar Shah:** Writing – review & editing, Supervision, Resources, Project administration, Conceptualization.

Declaration of competing interest

The authors declare that they have no known competing financial interests or personal relationships that could have appeared to influence the work reported in this paper.

Data availability

No data was used for the research described in the article.

Acknowledgement

The authors would like to thank Ulster University for supporting this research through PhD studentship funding from Northern Ireland Department for the Economy (DfE). The authors would like to acknowledge the Built Environment Research Institute for the financial support provided for the study. The central lab facility provided by the Nanotechnology and Integrated Bio-engineering Centre (NIBEC), Ulster University, and the UV–Vis–NIR spectroscopic facility provided by Prof. Davide Mariotti are also sincerely acknowledged. The help provided by Dr. Ruairi McGlynn in the XPS characterization process is also acknowledged.

Appendix A. Supplementary data

Supplementary data to this article can be found online at https://doi.org/10.1016/j.jclepro.2023.140395.

References

Abbasi, N.M., Xiao, Y., Zhang, L., Peng, L., Duo, Y., Wang, L., Yin, P., Ge, Y., Zhu, H., Zhang, B., Xie, N., Duan, Y., Wang, B., Zhang, H., 2021. Heterostructures of titanium-based MXenes in energy conversion and storage devices. J. Mater. Chem. C 9, 8395–8465. https://doi.org/10.1039/d1tc00327e.

Ahmadian-Fard-Fini, S., Salavati-Niasari, M., Ghanbari, D., 2018. Hydrothermal green synthesis of magnetic Fe3O4-carbon dots by lemon and grape fruit extracts and as a photoluminescence sensor for detecting of E. coli bacteria. Spectrochim. Acta Part A Mol. Biomol. Spectrosc. 203, 481–493. https://doi.org/10.1016/j.saa.2018.06.021.

Ambreen, T., Saleem, A., Park, C.W., 2022. Thermal efficiency of eco-friendly MXene based nanofluid for performance enhancement of a pin-fin heat sink: experimental and numerical analyses. Int. J. Heat Mass Tran. 186, 122451 https://doi.org/10.1016/j.ijheatmasstransfer.2021.122451.

Azizi, Z., Alamdari, A., Doroodmand, M.M., 2018. Highly stable copper/carbon dot nanofluid: preparation and characterization. J. Therm. Anal. Calorim. 133, 951–960. https://doi.org/10.1007/s10973-018-7293-9.

Bao, Z., Bing, N., Zhu, X., Xie, H., Yu, W., 2021. Ti3C2Tx MXene contained nanofluids with high thermal conductivity, super colloidal stability and low viscosity. Chem. Eng. J. 406, 126390 https://doi.org/10.1016/j.cej.2020.126390.

Biesinger, M.C., Lau, L.W.M., Gerson, A.R., Smart, R.S.C., 2010. Resolving surface chemical states in XPS analysis of first row transition metals, oxides and hydroxides: Sc, Ti, V, Cu and Zn. Appl. Surf. Sci. 257, 887–898. https://doi.org/10.1016/j.apsusc.2010.07.086.

Cao, Y., Deng, Q., Liu, Z., Shen, D., Wang, T., Huang, Q., Du, S., Jiang, N., Lin, C.Te, Yu, J., 2017. Enhanced thermal properties of poly(vinylidene fluoride) composites with ultrathin nanosheets of MXene. RSC Adv. 7, 20494–20501. https://doi.org/10.1039/C7RA00184C.

Das, L., Habib, K., Irshad, K., Saidur, R., Algarni, S., Alqahtani, T., 2022. Thermo-optical characterization of Therminol 55 based MXene–Al2O3 hybridized nanofluid and new correlations for thermal properties. Nanomaterials 12. https://doi.org/10.3390/nano12111862.

Das, L., Habib, K., Saidur, R., Aslfattahi, N., Yahya, S.M., Rubbi, F., 2020. Improved thermophysical properties and energy efficiency of aqueous ionic liquid/MXene nanofluid in a hybrid PV/T solar system. Nanomaterials 10, 1–26. https://doi.org/10.3390/nano10071372.

Dervishi, E., Ji, Z., Htoon, H., Sykora, M., Doorn, S.K., 2019. Raman spectroscopy of bottom-up synthesized graphene quantum dots: size and structure dependence. Nanoscale 11, 16571–16581. https://doi.org/10.1039/c9nr05345j.

Du, Y., Zhang, X., Wei, L., Yu, B., Ma, D., Ye, S., 2019. Electrodeposition of a Ni-P-TiO2/Ti3C2Tx coating with in situ grown nanoparticles TiO2 on Ti3C2Tx sheets. Coatings 9, 1–14. https://doi.org/10.3390/coatings9110750.

Ebrahimnia-Bajestan, E., Charjouei Moghadam, M., Niazmand, H., Daungthongsuk, W., Wongwises, S., 2016. Experimental and numerical investigation of nanofluids heat transfer characteristics for application in solar heat exchangers. Int. J. Heat Mass Tran. 92, 1041–1052. https://doi.org/10.1016/j.ijheatmasstransfer.2015.08.107.

Edison, T.N.J.I., Atchudan, R., Sethuraman, M.G., Shim, J.J., Lee, Y.R., 2016. Microwave assisted green synthesis of fluorescent N-doped carbon dots: cytotoxicity and bio-imaging applications. J. Photochem. Photobiol. B Biol. 161, 154–161. https://doi.org/10.1016/j.jphotobiol.2016.05.017.

Ettefaghi, E., Rashidi, A., Ghobadian, B., Najafi, G., Khoshtaghaza, M.H., Sidik, N.A.C., Yadegari, A., Xian, H.W., 2018. Experimental investigation of conduction and convection heat transfer properties of a novel nanofluid based on carbon quantum dots. Int. Commun. Heat Mass Tran. 90, 85–92. https://doi.org/10.1016/j.icheatmasstransfer.2017.10.002.

Feng, W., Luo, H., Wang, Y., Zeng, S., Tan, Y., Zhang, H., Peng, S., 2018. Ultrasonic assisted etching and delaminating of Ti3C2 Mxene. Ceram. Int. 44, 7084–7087. https://doi.org/10.1016/j.ceramint.2018.01.147.

Feng, X., Han, G., Cai, J., Wang, X., 2022. Au@Carbon quantum Dots-MXene nanocomposite as an electrochemical sensor for sensitive detection of nitrite. J. Colloid Interface Sci. 607, 1313–1322. https://doi.org/10.1016/j.jcis.2021.09.036.

Geng, B., Xu, S., Shen, L., Fang, F., Shi, W., Pan, D., 2021. Multifunctional carbon dot/MXene heterojunctions for alleviation of tumor hypoxia and enhanced sonodynamic therapy. Carbon N. Y. 179, 493–504. https://doi.org/10.1016/j.carbon.2021.04.070.

Ghafouri, A., Toghraie, D., 2023. Experimental study on thermal conductivity of SiC-ZnO/ethylene glycol hybrid nanofluid: proposing an optimized multivariate correlation. J. Taiwan Inst. Chem. Eng. 148, 104824 https://doi.org/10.1016/j.jtice.2023.104824.

Godson, L., Raja, B., Lal, D.M., Wongwises, S., 2010. Experimental investigation on the thermal conductivity and viscosity of silver-deionized water nanofluid. Exp. Heat Tran. 23, 317–332. https://doi.org/10.1080/08916150903564796.

Gou, L., Jing, W., Li, Y., Wang, M., Hu, S., Wang, H., He, Y.B., 2021. Lattice-coupled Si/MXene confined by hard carbon for fast sodium-ion conduction. ACS Appl. Energy Mater. 4, 7268–7277. https://doi.org/10.1021/acsaem.1c01396.

Hatimuria, M., Phukan, P., Bag, S., Ghosh, J., Gavvala, K., Pabbathi, A., Das, J., 2023. Green carbon dots: applications in development of electrochemical sensors, assessment of toxicity as well as anticancer properties. Catalysts 13. https://doi.org/10.3390/catal13030537.

Hot disk instruments, 2015. TPS 2500 S Brochure.

Hu, T., Wang, J., Zhang, H., Li, Z., Hu, M., Wang, X., 2015. Vibrational properties of Ti3C2 and Ti3C2T2 (T = O, F, OH) monosheets by first-principles calculations: a comparative study. Phys. Chem. Chem. Phys. 17, 9997–10003. https://doi.org/10.1039/c4cp05666c.

Huang, J., Han, X., Zhao, X., Khosa, A.A., Meng, C., 2022. The stability, optical behavior optimization of Ag@SiO2 nanofluids and their application in spectral splitting photovoltaic/thermal receivers. Renew. Energy 190, 865–878. https://doi.org/10.1016/j.renene.2022.03.146.

John, B.K., John, N., Mathew, S., Korah, B.K., Punnoose, M.S., Mathew, B., 2022. Fluorescent carbon quantum dots as a novel solution and paper strip-based dual sensor for the selective detection of Cr(VI) ions. Diam. Relat. Mater. 126, 109138 https://doi.org/10.1016/j.diamond.2022.109138.

Joseph, A., Thomas, S., 2022. Energy, exergy and corrosion analysis of direct absorption solar collector employed with ultra-high stable carbon quantum dot nanofluid. Renew. Energy 181, 725–737. https://doi.org/10.1016/j.renene.2021.09.079.

Kim, A., Dash, J.K., Kumar, P., Patel, R., 2022. Carbon-based quantum dots for photovoltaic devices: a review. ACS Appl. Electron. Mater. 4, 27–58. https://doi.org/10.1021/acsaelm.1c00783.

Krishnamoorthy, K., Pazhamalai, P., Sahoo, S., Kim, S.J., 2017. Titanium carbide sheet based high performance wire type solid state supercapacitors. J. Mater. Chem. A 5, 5726–5736. https://doi.org/10.1039/C6TA11198J.

Li, L., Jiang, G., An, C., Xie, Z., Wang, Y., Jiao, L., Yuan, H., 2020. Hierarchical Ti3C2@TiO2 MXene hybrids with tunable interlayer distance for highly durable lithium-ion batteries. Nanoscale 12, 10369–10379. https://doi.org/10.1039/d0nr01222j.

Li, S., Zhou, Q., Li, Z., Liu, M., Li, Y., Chen, C., 2023. Sensitive fluorescent probe based on combination of magnetic molecularly imprinted materials and carbon dots derived from prussian blue for p-aminoazobenzene in environmental samples. J. Clean. Prod. 402, 136827 https://doi.org/10.1016/j.jclepro.2023.136827.

Li, W., Song, Z., Zhong, J., Qian, J., Tan, Z., Wu, X., Chu, H., Nie, W., Ran, X., 2019. Multilayer-structured transparent MXene/PVDF film with excellent dielectric and energy storage performance. J. Mater. Chem. C 7, 10371–10378. https://doi.org/10.1039/c9tc02715g.

Li, X., Yin, X., Han, M., Song, C., Xu, H., Hou, Z., Zhang, L., Cheng, L., 2017. Ti3C2 MXenes modified with in situ grown carbon nanotubes for enhanced electromagnetic wave absorption properties. J. Mater. Chem. C 5, 4068–4074. https://doi.org/10.1039/c6tc05226f.

Mahesh, K.V., Linsha, V., Peer Mohamed, A., Ananthakumar, S., 2016. Processing of 2D-MAXene nanostructures and design of high thermal conducting, rheo-controlled MAXene nanofluids as a potential nanocoolant. Chem. Eng. J. 297, 158–169. https://doi.org/10.1016/j.cej.2016.04.010.

Meng, L., Ushakova, E.V., Zhou, Z., Liu, E., Li, D., Zhou, D., Tan, Z., Qu, S., Rogach, A.L., 2020. Microwave-assisted in situ large scale synthesis of a carbon dots@g-C3N4 composite phosphor for white light-emitting devices. Mater. Chem. Front. 4, 517–523. https://doi.org/10.1039/c9qm00659a.

Mirsaeidi, A.M., Yousefi, F., 2021. Viscosity, thermal conductivity and density of carbon quantum dots nanofluids: an experimental investigation and development of new correlation function and ANN modeling. J. Therm. Anal. Calorim. 143, 351–361. https://doi.org/10.1007/s10973-019-09138-z.

Mousavi, S.M., Esmaeilzadeh, F., Wang, X.P., 2019. Effects of temperature and particles volume concentration on the thermophysical properties and the rheological behavior of CuO/MgO/TiO2 aqueous ternary hybrid nanofluid: experimental investigation. J. Therm. Anal. Calorim. 137, 879–901. https://doi.org/10.1007/s10973-019-08006-0.

Naguib, M., Mashtalir, O., Lukatskaya, M.R., Dyatkin, B., Zhang, C., Presser, V., Gogotsi, Y., Barsoum, M.W., 2014. One-step synthesis of nanocrystalline transition metal oxides on thin sheets of disordered graphitic carbon by oxidation of MXenes. Chem. Commun. 50, 7420–7423. https://doi.org/10.1039/c4cc01646g.

Niu, W.J., Li, Y., Zhu, R.H., Shan, D., Fan, Y.R., Zhang, X.J., 2015. Ethylenediamine-assisted hydrothermal synthesis of nitrogen-doped carbon quantum dots as fluorescent probes for sensitive biosensing and bioimaging. Sensor. Actuator. B Chem. 218, 229–236. https://doi.org/10.1016/j.snb.2015.05.006.

Parashar, N., Aslfattahi, N., Yahya, S.M., Saidur, R., 2021. ANN modeling of thermal conductivity and viscosity of MXene-based aqueous ionanofluid. Int. J. Thermophys. 42, 1–24. https://doi.org/10.1007/s10765-020-02779-5.

Pesteei, S.M., Subbarao, P.M.V., Agarwal, R.S., 2005. Experimental study of the effect of winglet location on heat transfer enhancement and pressure drop in fin-tube heat exchangers, 25, pp. 1684–1696. https://doi.org/10.1016/j.applthermaleng.2004.10.013.

Rub Pakkath, S.A., Chetty, S.S., Selvarasu, P., Vadivel Murugan, A., Kumar, Y., Periyasamy, L., Santhakumar, M., Sadras, S.R., Santhakumar, K., 2018. Transition metal ion (Mn2+,Fe2+,Co2+, and Ni2+)-doped carbon dots synthesized via microwave-assisted pyrolysis: a potential nanoprobe for magneto-fluorescent dual-modality bioimaging. ACS Biomater. Sci. Eng. 4, 2581–2596. https://doi.org/10.1021/acsbiomaterials.7b00943.

Said, Z., Sharma, P., Aslfattahi, N., Ghodbane, M., 2022. Experimental analysis of novel ionic liquid-MXene hybrid nanofluid's energy storage properties: model-prediction using modern ensemble machine learning methods. J. Energy Storage 52, 104858. https://doi.org/10.1016/j.est.2022.104858.

Said, Z., Sohail, M.A., Pandey, A.K., Sharma, P., Waqas, A., Chen, W.H., Nguyen, P.Q.P., Nguyen, V.N., Pham, N.D.K., Nguyen, X.P., 2023. Nanotechnology-integrated phase change material and nanofluids for solar applications as a potential approach for clean energy strategies: progress, challenges, and opportunities. J. Clean. Prod. 416, 137736 https://doi.org/10.1016/j.jclepro.2023.137736.

Sandhu, H., Gangacharyulu, D., 2017. An experimental study on stability and some thermophysical properties of multiwalled carbon nanotubes with water–ethylene glycol mixtures. Part. Sci. Technol. 35, 547–554. https://doi.org/10.1080/02726351.2016.1180335.

Selvaraj, V., Krishnan, H., 2021. Graphene-silver alloyed quantum dots nanofluid: synthesis and application in the cooling of a simulated electronic system. Appl. Therm. Eng. 187, 116580 https://doi.org/10.1016/j.applthermaleng.2021.116580.

Sengupta, A., Rao, B.V.B., Sharma, N., Parmar, S., Chavan, V., Singh, S.K., Kale, S., Ogale, S., 2020. Comparative evaluation of MAX, MXene, NanoMAX, and NanoMAX-derived-MXene for microwave absorption and Li ion battery anode applications. Nanoscale 12, 8466–8476. https://doi.org/10.1039/c9nr10980c.

Shahrul, I.M., Mahbubul, I.M., Khaleduzzaman, S.S., Saidur, R., Sabri, M.F.M., 2014. A comparative review on the specific heat of nanofluids for energy perspective. Renew. Sustain. Energy Rev. 38, 88–98. https://doi.org/10.1016/j.rser.2014.05.081.

Shaikh, A.F., Tamboli, M.S., Patil, R.H., Bhan, A., Ambekar, J.D., Kale, B.B., 2018. Bioinspired carbon quantum dots: an antibiofilm agents. J. Nanosci. Nanotechnol. 19, 2339–2345. https://doi.org/10.1166/jnn.2019.16537.

Siddiqui, F.R., Tso, C.Y., Chan, K.C., Fu, S.C., Chao, C.Y.H., 2019. On trade-off for dispersion stability and thermal transport of Cu-Al2O3 hybrid nanofluid for various mixing ratios. Int. J. Heat Mass Tran. 132, 1200–1216. https://doi.org/10.1016/j.ijheatmasstransfer.2018.12.094.

Sreekumar, S., Joseph, A., Kumar, C.S.S., Thomas, S., 2019. Investigation on influence of antimony tin oxide/silver nanofluid on direct absorption parabolic solar collector. J. Clean. Prod., 119378 https://doi.org/10.1016/j.jclepro.2019.119378.

Sreekumar, S., Shah, N., Mondol, J., Hewitt, N., Chakrabarti, S., 2022a. Broadband absorbing mono, blended and hybrid nanofluids for direct absorption solar collector: a comprehensive review. Nano Futures. https://doi.org/10.1088/2399-1984/ac57f7.

Sreekumar, S., Shah, N., Mondol, J.D., Hewitt, N., Chakrabarti, S., 2022b. Broadband absorbing mono, blended and hybrid nanofluids for direct absorption solar collector: a comprehensive review. Nano Futures. https://doi.org/10.1088/2399-1984/ac57f7.

Sun, X., He, J., Meng, Y., Zhang, L., Zhang, S., Ma, X., Dey, S., Zhao, J., Lei, Y., 2016. Microwave-assisted ultrafast and facile synthesis of fluorescent carbon nanoparticles from a single precursor: preparation, characterization and their application for the highly selective detection of explosive picric acid. J. Mater. Chem. A 4, 4161–4171. https://doi.org/10.1039/c5ta10027e.

Swamy, V., Kuznetsov, A., Dubrovinsky, L.S., Caruso, R.A., Shchukin, D.G., Muddle, B.C., 2005. Finite-size and pressure effects on the Raman spectrum of nanocrystalline anatase TiO2. Phys. Rev. B Condens. Matter 71, 184302. https://doi.org/10.1103/PhysRevB.71.184302.

Vatani, A., Woodfield, P.L., Kim, T.H., Lemckert, C., Li, Q., Dao, D., 2019. Apparent thermal conductivity of photoluminescent C-dot nanofluid. J. Mol. Liq. 286 https://doi.org/10.1016/j.molliq.2019.110948.

Wang, B.X., Zhou, L.P., Peng, X.F., 2006. Surface and size effects on the specific heat capacity of nanoparticles. Int. J. Thermophys. 27, 139–151. https://doi.org/10.1007/s10765-006-0022-9.

Wang, L., Zhang, H., Wang, B., Shen, C., Zhang, C., Hu, Q., Zhou, A., Liu, B., 2016. Synthesis and electrochemical performance of Ti3C2Tx with hydrothermal process. Electron. Mater. Lett. 12, 702–710. https://doi.org/10.1007/s13391-016-6088-z.

Wang, Y., Li, Y., Qiu, Z., Wu, X., Zhou, P., Zhou, T., Zhao, J., Miao, Z., Zhou, J., Zhuo, S., 2018. Fe3O4@Ti3C2 MXene hybrids with ultrahigh volumetric capacity as an anode material for lithium-ion batteries. J. Mater. Chem. A 6, 11189–11197. https://doi.org/10.1039/c8ta00122g.

Wen, Y., Ma, C., Wei, Z., Zhu, X., Li, Z., 2019. FeNC/MXene hybrid nanosheet as an efficient electrocatalyst for oxygen reduction reaction. RSC Adv. 9, 13424–13430. https://doi.org/10.1039/c9ra01330j.

Xiao, Y., Bao, Y., Yu, L., Zheng, X., Qin, G., Chen, M., He, M., 2023. Ultra-stable carbon quantum dot nanofluids as excellent spectral beam splitters in PV/T applications. Energy 273, 127159. https://doi.org/10.1016/j.energy.2023.127159.

Xiong, Q., Hajjar, A., Alshuraiaan, B., Izadi, M., Altnji, S., Shehzad, S.A., 2021. State-of-the-art review of nanofluids in solar collectors: a review based on the type of the dispersed nanoparticles. J. Clean. Prod. 310, 127528 https://doi.org/10.1016/j.jclepro.2021.127528.

Xuan, Z., Zhai, Y., Li, Y., Li, Z., Wang, H., 2022. Guideline for selecting appropriate mixing ratio of hybrid nanofluids in thermal management systems. Powder Technol. 403, 117425 https://doi.org/10.1016/j.powtec.2022.117425.

Zhang, T., Pan, L., Tang, H., Du, F., Guo, Y., Qiu, T., Yang, J., 2017. Synthesis of two-dimensional Ti3C2TxMXene using HCl+LiF etchant: enhanced exfoliation and delamination. J. Alloys Compd. 695, 818–826. https://doi.org/10.1016/j.jallcom.2016.10.127.

Zhang, W., Zhang, X., 2022. The effect of ultrasound on synthesis and energy storage mechanism of Ti3C2Tx MXene. Ultrason. Sonochem. 89, 106122 https://doi.org/10.1016/j.ultsonch.2022.106122.

Zheng, W., Zhang, P., Chen, J., Tian, W.B., Zhang, Y.M., Sun, Z.M., 2018. In situ synthesis of CNTs@Ti3C2 hybrid structures by microwave irradiation for high-performance anodes in lithium ion batteries. J. Mater. Chem. A 6, 3543–3551. https://doi.org/10.1039/c7ta10394h.

Zheng, W., Zhang, P.G., Chen, J., Tian, W.B., Zhang, Y.M., Sun, Z.M., 2019. Microwave-assisted synthesis of three-dimensional MXene derived metal oxide/carbon nanotube/iron hybrids for enhanced lithium-ions storage. J. Electroanal. Chem. 835, 205–211. https://doi.org/10.1016/j.jelechem.2019.01.036.

Zhou, S.Q., Ni, R., 2008. Measurement of the specific heat capacity of water-based Al2O3 nanofluid. Appl. Phys. Lett. 92, 1–4. https://doi.org/10.1063/1.2890431.